

Copyright

by

Brandon Paul Smith

2016

**The Thesis Committee for Brandon Paul Smith  
Certifies that this is the approved version of the following thesis:**

**Four-Probe Measurements of Anisotropic In-Plane Thermal  
Conductivities of Thin Black Phosphorus**

**APPROVED BY  
SUPERVISING COMMITTEE:**

**Supervisor:**

---

Li Shi

---

Deji Akinwande

**Four-Probe Measurements of Anisotropic In-Plane Thermal  
Conductivities of Thin Black Phosphorus**

**by**

**Brandon Paul Smith, B.S.**

**Thesis**

Presented to the Faculty of the Graduate School of

The University of Texas at Austin

in Partial Fulfillment

of the Requirements

for the Degree of

**Master of Science in Engineering**

**The University of Texas at Austin**

**August 2016**

## **ACKNOWLEDGEMENTS**

I would first like to thank my family and friends for their unconditional love and support. I would like to thank Jaehyun Kim for always finding time to help and teach me. Similarly, I would like to thank Eric Ou for the troubleshooting sessions and countless discussions. I thank the Cockrell School of Engineering for their generous financial support. I owe incredible gratitude to Dr. Shi for his constant patience, guidance, and encouragement. I am enormously thankful to work in the Li Shi Group where there is sincere passion for science that translates into an innovative and gritty research environment.

## **Abstract**

### **Four-Probe Measurements of Anisotropic In-Plane Thermal Conductivities of Thin Black Phosphorus**

Brandon Paul Smith, M.S.E.

The University of Texas at Austin, 2016

Supervisor: Li Shi

Phosphorene, a two-dimensional material exfoliated from black phosphorus (BP), is a promising p-type, high-mobility semiconductor. Phosphorene and BP display intrinsic in-plane anisotropic transport properties due to its puckered honeycomb lattice with distinct armchair and zigzag crystallographic orientations. The anisotropic thermal transport properties of BP and phosphorene influence the performance and reliability of functional devices made from these materials, and remain to be better understood. Here, we report the anisotropic in-plane thermal conductivities of suspended multi-layer BP samples, which are measured by a four-probe thermal transport measurement method. The measurement device consists of four microfabricated, suspended Pd/SiN<sub>x</sub> lines that act as resistive heaters and thermometers. The BP flake is suspended across the microstructure in contact with all four lines. This four-probe thermal transport measurement is equipped with the unique ability to isolate the intrinsic thermal resistance from the contact thermal resistance, which can be a major source of error in thermal conductivity measurements of

nanostructures. Four BP samples were measured with thicknesses ranging from 39.2 nm to 274 nm and a peak thermal conductivity of  $142 \text{ W m}^{-1} \text{ K}^{-1}$  at 80 K for a 55.6 nm thick zigzag-oriented flake. The measurement results exhibit more pronounced temperature dependence with a higher peak thermal conductivity together with a weaker thickness dependence than prior reports. The results suggest the important role of defects in thermal transport in thin BP flakes, which can degrade upon exposure to air and water.

## Table of Contents

Abstract .....	v
List of Tables .....	viii
List of Figures .....	ix
Chapter 1: Introduction .....	1
1.1 Black Phosphorus .....	3
1.1.1 Thermal Transport Measurement Techniques .....	5
1.2 Motivation of This Work.....	8
Chapter 2: Four-Probe Thermal Measurement .....	10
2.1 Four-Probe Microdevice .....	10
2.2 Finite Width Derivation .....	12
2.3 Sample Assembly .....	18
2.3.1 BP Exfoliation and Transfer .....	19
2.3.2 Sample Preparation.....	19
2.4 Measurement Process .....	20
2.5 Characterization Results.....	22
2.6 Uncertainty Analysis .....	27
Chapter 3: Results and Discussion.....	30
3.1 Experimental Results.....	30i
3.2 Temperature and Thickness Dependence.....	35
Chapter 4: Conclusion.....	45
References .....	47

## List of Tables

<b>Table 2.1.</b> Device dimensions for measured samples. ....	18
<b>Table 2.2.</b> Sample dimensions of the middle suspended segment and their uncertainty. ....	28
<b>Table 3.1.</b> Average, high, and low contact resistance values for the two middle beams for the 39.2 nm, 55.6 nm, and 145 nm thick BP flakes. ....	34

## List of Figures

**Figure 1.1.** Black phosphorus crystal structure illustration displaying the in-plane crystallographic axes and three Raman-active vibrational modes. .... 4

**Figure 2.1.** Thermal resistance circuit of the measurement device when the first Pd/Cr line is electrically heated at a rate of  $(IV)_1$ .  $R_1$ ,  $R_2$ , and  $R_3$  are the intrinsic thermal resistances of the left, middle, and right suspended segments of the suspended black phosphorus sample.  $R_{c,j}$  is the contact thermal resistance between the  $j^{\text{th}}$  Pd/SiN<sub>x</sub> line and the sample.  $R_{b,j}$  is the thermal resistance of the  $j^{\text{th}}$  Pd/Cr resistance thermometer line.  $\theta_{c,j,i}$  is the  $j^{\text{th}}$  Pd/Cr line temperature rise at the contact to the sample when the  $i^{\text{th}}$  line is used as the heater line. The temperature rise  $\theta_0$  at the two ends of each of the suspended Pd/Cr lines is assumed to be negligible.<sup>57</sup> ..... 11

**Figure 2.2.** (a) Optical micrograph of a 55.6 nm thick, 2.46  $\mu\text{m}$  wide BP sample assembled across four suspended Pd/Cr lines together with a schematic of the temperature profiles along the Pd/Cr heat line ( $i^{\text{th}}$  line) and one Pd/SiN<sub>x</sub> resistance thermometer line ( $j^{\text{th}}$  line,  $j \neq i$ ). (b) Tilted SEM image of a 39.2 nm thick BP flake displaying typical contact of a BP sample to a Pd/Cr line. Scale bars are 5  $\mu\text{m}$  for (a) and 1  $\mu\text{m}$  for (b). ..... 13

**Figure 2.3.** Top-down SEMs of measured BP flakes with thickness of (a) 39.2 nm, (b) 55.6 nm, (c) 145 nm, (d) 274 nm. Scale bar is 5  $\mu\text{m}$  (a-c) and 10  $\mu\text{m}$ . ..... 22

**Figure 2.4.** AFM height data used to obtain thicknesses of (a) 39.2 nm, (b) 55.6 nm, and (c) 145 nm via step function in the Nanoscope software package. .... 24

**Figure 2.5.** 85° tilted SEM of 274 nm thick BP flake used to obtain thickness in conjunction with other images. Scale bar is 1  $\mu\text{m}$ . .... 24

**Figure 2.6.** Typical Raman spectra for BP. .... 26

**Figure 2.7.** Angle-resolved polarized Raman spectra for two samples showing the lattice orientation dependence of the  $Ag_2$  to  $Ag_1$  intensity ratio. The lines are simple fitting to the measurement results (symbols). The rotation angles of 90° and 180° correspond to light polarization perpendicular and parallel, respectively, to the heat transport direction along the sample. .... 26

**Figure 3.1.** Pd/Cr line thermal resistance as a function of temperature for 145 nm thick BP sample. The error bars of some of the data are smaller than the symbol size. .... 30

**Figure 3.2.** Thermal resistances as a function of temperature for (a) 39.2 nm, (b) 55.6 nm, (c) 145 nm, and (d) 274 nm thick BP samples. The error bars of some of the data are smaller than the symbol size. .... 33

**Figure 3.3.** In-plane thermal conductivity of suspended few-layer black phosphorus for samples oriented along the AC (blue) and ZZ (red) direction. The error bars of some of the data are smaller than the symbol size. .... 37

**Figure 3.4.** Temperature dependence of the basal-plane thermal conductivities of the BP samples measured in this work (filled symbols) and in a recent report by Lee et al.<sup>34</sup> (unfilled symbols) for the zigzag (a) and the armchair (b) directions. The dashed lines are the theoretical calculation results for defect-free samples. The solid lines are the calculation results with additional phonon scattering by vacancy point defects at a concentration of 0.04%, 0.145%, 0.1%, and 0.14%, respectively for the 55.6 nm, 274 nm, 145 nm, and 39.2 nm samples, 0.6% and 0.4 % for the 170 nm thick, zigzag-oriented and armchair-oriented samples of Lee et al.,<sup>34</sup> respectively. The dashed and solid lines are provided by collaborators Bjorn Vermeersch, Jesús Carrete, and Natalio Mingo. The sample thickness is indicated in the legend. The error bars of some of the data from this work are smaller than the symbol size. .... 39

**Figure 3.5.** Thickness dependence of the room-temperature thermal conductivities of the BP samples measured in this work (filled circles), by Luo et al.<sup>33</sup> with micro-Raman thermometry (unfilled diamond symbols), by Lee et al.<sup>34</sup> with a two-probe method (unfilled square symbols), and by Jang et al.<sup>35</sup> using TDTR (crosses) for the zigzag (a, red symbols) direction and the armchair (b, blue symbols) and through-plane direction (b, black crosses) directions. The dashed and solid lines are the calculation results for defect-free samples and samples with 0.1% point vacancies, respectively, provided by collaborators Bjorn Vermeersch, Jesús Carrete, and Natalio Mingo. .... 40

## Chapter 1: Introduction

Since the creation of the solid state transistor by John Bardeen, Walter Brattain, and William Shockley in 1947 and the subsequent creation of the integrated circuit by Jack Kilby in 1958, the computer electronics industry has pursued an insistent path to maximize processing power while reducing cost. This drive has primarily been achieved by increasing device density that has generally followed Moore's Law,<sup>1</sup> which states the number of transistors in an integrated circuit chip doubles every 18-24 months, and progressive device miniaturization where the characteristic dimension of the device has shrunk from the macroscale into the nanoscale.

Increasing device density and reducing logic gate size have the negative effect of increasing power density across all scales of the system.<sup>2,3</sup> Power density is directly related to the generation of heat that must be dissipated or transported out of the system in order for operation of electronics at peak performance, which occurs at maximum power. In solids, heat is transported by charge carriers such as electrons and holes or by phonons, which are quantized atomic lattice vibrations. For semiconductors and insulators, the thermal conductivity,  $\kappa$ , is dominated by phonon transport, whereas in metals the contribution by charged carriers exceed lattice vibrations. Electronic device performance, power density, and thermal management critically depend on understanding the thermal conductivity of its base components.

The importance of R&D and innovation in the computer electronics industry coupled with heightened interest in low-dimensional nanomaterials has resulted in the emergent field of flexible electronics.<sup>4</sup> These devices are fabricated by creating logic devices from two-dimensional (2D) nanomaterials on a flexible substrate.<sup>5-8</sup> The use of 2D crystals are essential to obtain overall device flexibility due to their superior strain limits, which experimentally exceeds 20%, compared to conventional bulk semiconductor materials.<sup>4,9</sup> An example of a flexible electronic device has been illustrated in a recent review by the Akinwande et al. on flexible nanoelectronics.<sup>4</sup> The requirement of substrate flexibility is met by soft polymers or plastics, which have a thermal conductivity two orders of magnitude lower than their bulk silicon semiconductor counterpart. Additionally, polymers and plastics have melting temperatures below practical device operating temperatures. Hence, power density limitations and thermal management challenges are exacerbated in flexible electronics. A recent publication by Akinwande<sup>4</sup> has described flexible device failure due to hotspot generation from high power density. For this reason, there is great desire to find 2D nanomaterials with efficient, enhanced heat spreading capabilities to obtain high performance flexible electronics.<sup>3,4,10</sup>

## 1.1 Black Phosphorus

The rediscovery of graphene by Nobel Prize winners Andre Geim and Konstantin Novoselov inspired the resurgence of 2D nanomaterial research worldwide.<sup>11</sup> This enthusiasm combined with graphene's shortcoming of zero bandgap has led to advances in other 2D nanomaterials, including transition metal dichalcogenides (TMDs) and hexagonal boron nitride (h-BN).<sup>4</sup> TMD are of the form  $\text{MX}_2$  where M is a transition metal atom (Mo, W, etc.) and X a chalcogen atom (S, Se, or Te).<sup>12,13</sup> h-BN is an ideal 2D dielectric and a possible heat dissipater in flexible electronics.<sup>14,15</sup> In addition, 2D puckered or buckled crystals have been termed Xenes, which include silicene,<sup>16</sup> germanene,<sup>17</sup> and phosphorene.<sup>18-21</sup>

Phosphorene, a stable allotrope of phosphorus at ambient pressure and temperature, is a 2D monolayer exfoliated from black phosphorus (BP) in 2014.<sup>18-21</sup> Due to weak interlayer bonding, multi-layer BP flakes can be mechanically exfoliated from bulk crystals for use in electronic and optoelectronic applications.<sup>18-22</sup> Compared to graphene and TMDs,<sup>4,23</sup> BP has distinct electrical and thermal transport anisotropy arising from its puckered honeycomb structure.<sup>18,24</sup> This anisotropy along BP's two high-symmetry, in-plane directions has been theoretically and experimentally examined for mechanical,<sup>25,26</sup> optical,<sup>20,27,28</sup> electrical,<sup>18-22,24,27,29</sup> and thermal properties.<sup>24,29-36</sup> The aforementioned high-symmetry, in-plane crystallographic axes are referred to as the zigzag (ZZ) and armchair (AC) directions where ZZ is along the  $a$ -axis and AC is along the  $c$ -axis with lattice

constants of 3.314 Å and 4.376 Å, respectively.<sup>27</sup> The thickness-dependent thermal conductivity of BP has been calculated only under the relaxation-time approximation and using boundary scattering models developed for isotropic crystals, which is inherently incorrect due to the distinct anisotropy of BP.<sup>33</sup>

BP's distinct ZZ and AC directions can be determined with angle-resolved polarized Raman spectroscopy. BP has three observable Raman-active vibrational modes at  $\approx 363 \text{ cm}^{-1}$  ( $A_g^1$ ),  $\approx 440 \text{ cm}^{-1}$  ( $B_{2g}$ ), and  $\approx 467 \text{ cm}^{-1}$  ( $A_g^2$ ).<sup>37,38</sup> BP crystal structure and its observable vibrational modes are shown in Figure 1.1 where the  $A_g^1$ ,  $B_{2g}$ , and  $A_g^2$  modes correspond to vibrations along the [010] (out of plane), [100] (in-plane, ZZ), and [001] (in-plane, AC) directions, respectively. The intensities of the  $A_g^1$ ,  $B_{2g}$ , and  $A_g^2$  modes can be used to determine the crystal orientation because they are functions of the laser polarization direction with respect to the  $a$ - $c$  plane.<sup>38</sup> Specifically, the intensity ratio of the  $A_g^2$  mode to the  $A_g^1$  mode reaches its maximum when the Raman laser is polarized in parallel to the AC direction.<sup>20</sup>

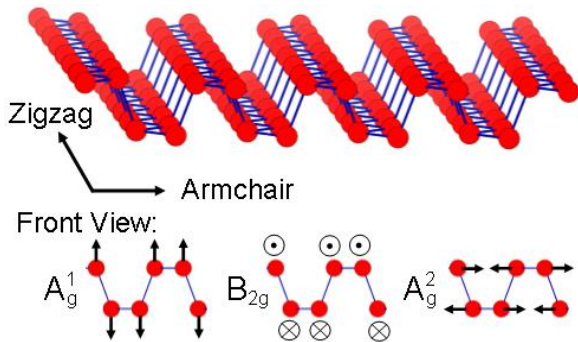


**Figure 1.1.** Black phosphorus crystal structure illustration displaying the in-plane crystallographic axes and three Raman-active vibrational modes.

Exfoliated BP flakes chemically degrade upon exposure to an ambient environment.<sup>39-41</sup> BP is hygroscopic and reacts with O<sub>2</sub> saturated H<sub>2</sub>O to produce PO<sub>x</sub> species causing irreversible alteration of material and electronic properties.<sup>39,41</sup> Additionally, light exposure increases the chemical reactivity of BP with O<sub>2</sub>.<sup>40</sup> Volume increase due to water absorption and layer-by-layer etching characterize the deterioration process. Topographic protrusions or bubbles form on the top layer that can be quantified by atomic force microscopy (AFM). This degradation can be substantially minimized with an atomic layer deposition of a thin AlO<sub>x</sub> passivation layer or by storage and measurement at high vacuum.

### **1.1.1 Thermal Transport Measurement Techniques**

A variety of thermal measurement methods have been developed to measure nanoscale materials due to their size-dependent unique thermal transport properties and increasing importance of thermal management for small-scale devices. The thermal conductivity of BP has been experimentally measured via micro-Raman thermometry,<sup>33</sup> two-probe microdevice,<sup>34</sup> time-domain thermoreflectance,<sup>35</sup> and the time-resolved magneto-optical Kerr effect.<sup>36</sup> BP thermal conductivity is dominated by lattice vibrations (phonons) along with a negligible electronic contribution.<sup>34,42</sup>

Raman thermometry has been used to investigate the thermal transport of properties of graphene,<sup>43</sup> carbon nanotubes,<sup>44</sup> h-BN,<sup>45</sup> and MoS<sub>2</sub>.<sup>46</sup> This method utilizes Raman spectroscopy to probe the sample temperature while simultaneously heating the sample

either by Joule heating or laser heating. The temperature rise modifies the optical phonon frequency causing a measurable red shift of the peaks. The thermal conductivity of the sample is extracted by solving a three-dimensional anisotropic heat conduction equation and matching the measured temperature and sample geometry. Raman thermometry suffers from limited temperature sensitivities, and strain shifts of Raman peaks, and heat loss to the surrounding gas molecules if the measurement is not carried out with the sample in vacuum. These effects can result in large thermal conductivity errors.

Suspended resistance thermometer two-probe microdevices have been used to measure carbon nanotubes,<sup>47,48</sup> silicon nanowires,<sup>49</sup> graphene,<sup>50</sup> and MoS<sub>2</sub>.<sup>51</sup> The device consists of two suspended silicon nitride (SiN<sub>x</sub>) pads that each contain serpentine platinum resistance thermometers connected to the bulk substrate by six SiN<sub>x</sub> beams. The pair of resistance thermometers act as both heaters and thermometers. A sample is suspended across the device so that it makes contact with the two membranes. The thermal resistance of the sample is determined by measuring the temperature rise in the two membranes while one membrane is heated. The extracted thermal resistance of the sample may contain error due to the presence of the contact thermal resistance. Contact resistance between the sample and measurement device can be evaluated by a four-probe method developed by Mavrokefalos et al. if the sample has a large, uniform Seebeck coefficient for both the suspended and supported segments.<sup>52</sup> This technique uses the nanofilm itself as a differential thermocouple to measure temperature drops. It is important to note that the supporting substrate may alter the electrical conductivity and Seebeck coefficient of

atomically thick samples, invalidating the assumption behind the four-probe method. Thermal conductivity is obtained from the measured thermal resistance after sample dimensions are evaluated

Time-domain thermoreflectance (TDTR) is similar to Raman thermometry in that a laser is used as both a pump and probe. However, the TDTR technique measures the change in reflectance of a material as its temperature changes. This transient method is best suited for cross-plane thermal transport measurements of thin films and interfaces.<sup>53,54</sup> In-plane thermal measurements of samples that lack in-plane crystal symmetry require the use of a beam-offset method.<sup>55</sup> The sample under investigation is coated with a thin, optically opaque metal transducer layer with known properties. An ultrafast laser is then split into a pump and probe used for heating and measuring, respectively. At the same location, the pump and probe reflect off the transducer layer into a photodetector. The probe beam measures the transient reflectivity response of the metal transducer caused by temperature change. Because the reflectivity of the transducer metal is known, the transient temperature change can be obtained and used to extract the thermal conductivity. There is limited sensitivity for the measurement of in-plane thermal conductivity of thin films if the thin film lateral thermal conductance is comparable to that of the substrate within the penetration depth. Moreover, the beam-offset method cannot measure monolayer or few-layer samples. Lastly, the smallest dimension of the sample needs to be larger than the micron-scale laser spot size, and the sample needs to have minimal surface roughness.

The time-resolved magneto-optical Kerr effect (TR-MOKE) measurement is fundamentally similar to the beam-offset TDTR measurement whereby laser pulses in the pump beam heat the sample surface while a temperature-dependent property is measured with a time-delayed probe beam.<sup>54</sup> TR-MOKE is different than TDTR in that the probe beam measures the temperature dependence of the polarization of reflected light as opposed to the intensity of reflected light.<sup>56</sup> The magneto-optical Kerr effect is responsible for rotating the polarization of the reflected probe beam. TR-MOKE allows the use of a non-optically opaque thin metal transducer layer.

## **1.2 Motivation of This Work**

This work investigates anisotropic thermal transport in few-layer black phosphorus along its two in-plane directions utilizing a new four-probe thermal transport measurement method developed by Kim et al., which has been used to measure silicon nanowires and boron arsenide microwires.<sup>57,58</sup> This four-probe microdevice is able to isolate contact thermal resistance from the intrinsic thermal resistance of a sample. Although three different experimental techniques have been used for black phosphorus thermal conductivity measurements, each measurement has difficulty in separating the contact thermal resistance from the intrinsic thermal resistance of the sample.

The intrinsic thermal conductivity of few-layer black phosphorus will provide useful data for the design of next-generation electronic devices such as flexible systems where thermal management is a major concern. This work presents black phosphorus

assembly onto the suspended four-probe microdevice, measurement of the intrinsic thermal resistance of four few-layer BP samples, and their characterization to obtain thermal conductivity results. The measurement results are compared with prior reports and collaborative theoretical calculation to develop a better understanding of the unusual thermal transport properties of BP and phosphorene.

## Chapter 2: Four-Probe Thermal Measurement

### 2.1 Four-Probe Microdevice

In the four-probe thermal transport measurement,<sup>57</sup> the nanostructure sample is suspended across four palladium/chromium/silicon nitride (Pd/Cr/SiN<sub>x</sub>) beams, which serve as resistive heaters and thermometers. The sample is placed on an evacuated sample stage of a variable temperature cryostat. One of the four lines is electrically heated while the electrical resistances of the four lines are measured. Based on the electrical resistance of each line measured without a heating current at different cryostat temperatures, the change in resistance versus temperature of each line due to the heating is used to obtain the average temperature rise in each line. A total of sixteen temperature measurements are obtained after each line has been used as the resistive heater. The sixteen measurement data can be used to obtain nine of the eleven thermal resistances shown in the thermal circuit of Figure 2.1. Because the heat flow rate in the middle suspended segment and across the two middle contacts are different and their ratios depend on which line is used as the heating line, the measurements obtain the middle suspended segment thermal resistance ( $R_2$ ) and the two contact thermal resistances ( $R_{c,2}$  and  $R_{c,3}$ ) to the middle suspended segment.

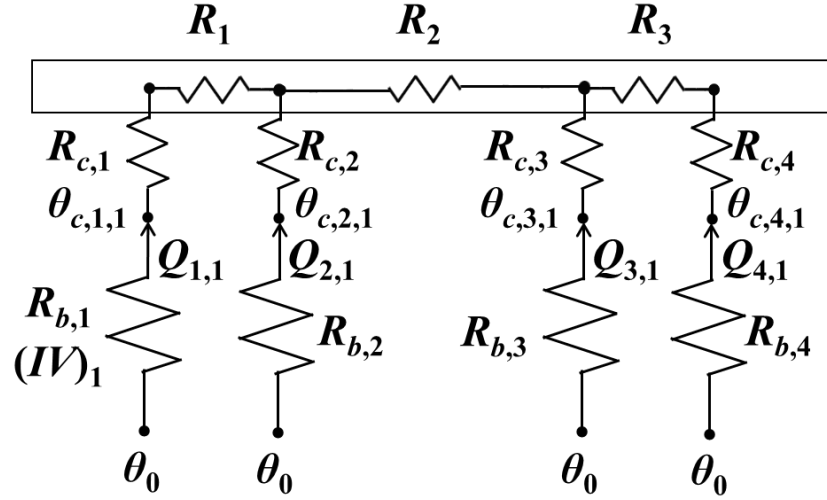


**Figure 2.1.** Thermal resistance circuit of the measurement device when the first Pd/Cr line is electrically heated at a rate of  $(IV)_1$ .  $R_1$ ,  $R_2$ , and  $R_3$  are the intrinsic thermal resistances of the left, middle, and right suspended segments of the suspended black phosphorus sample.  $R_{c,j}$  is the contact thermal resistance between the  $j^{\text{th}}$  Pd/SiN<sub>x</sub> line and the sample.  $R_{b,j}$  is the thermal resistance of the  $j^{\text{th}}$  Pd/Cr resistance thermometer line.  $\theta_{c,j,i}$  is the  $j^{\text{th}}$  Pd/Cr line temperature rise at the contact to the sample when the  $i^{\text{th}}$  line is used as the heater line. The temperature rise  $\theta_0$  at the two ends of each of the suspended Pd/Cr lines is assumed to be negligible.<sup>57</sup>

From the thermal circuit, the following three equations are used to obtain  $R_2$ ,  $R_{c,2}$ ,  $R_{c,3}$ ,  $R_1+R_{c,1}$ , and  $R_3+R_{c,4}$ :

$$\theta_{c,2,i} - \theta_{c,3,i} = Q_{2,i}R_{c,2} + (Q_{1,i} + Q_{2,1})R_2 - Q_{3,i}R_{c,3}, \text{ for } i = 1,2,3,4 \quad (2.1)$$

$$\theta_{c,1,i} - \theta_{c,2,i} = Q_{1,i}(R_1 + R_{c,1}) - Q_{2,i}R_{c,2}, \text{ for } i = 1,2,3,4 \quad (2.2)$$

$$\theta_{c,4,i} - \theta_{c,3,i} = Q_{4,i}(R_3 + R_{c,4}) - Q_{3,i}R_{c,3}, \text{ for } i = 1,2,3,4 \quad (2.3)$$

where the temperature rises and heat flow rates at different contacts can be obtained from the measured average temperature rise data, as discussed below.

## 2.2 Finite Width Derivation

The four-probe measurement performed in this work differs from the measurement created by Kim et al.<sup>57</sup> in that point contact between the BP and suspended Pd/Cr resistance thermometer line is not assumed. As a result, the finite width of the sample participates in heat conduction with temperature profiles of the  $i^{th}$  heating line and  $j^{th}$  resistance thermometer line illustrated in Figure 2.2(a). Figure 2.2(b) shows the conformal contact of BP to a Pd/Cr line.

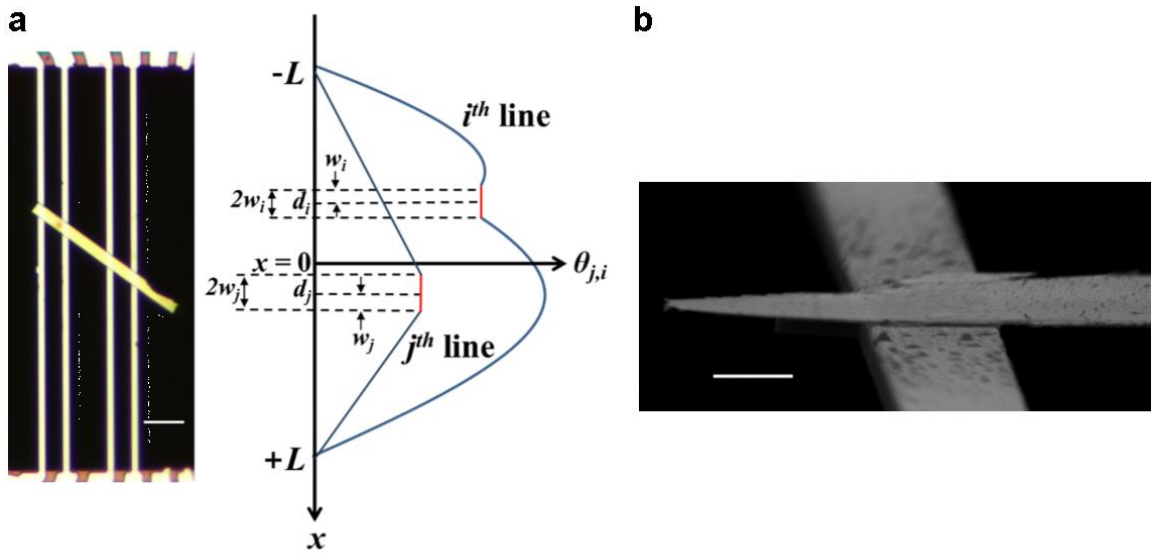


**Figure 2.2.** (a) Optical micrograph of a 55.6 nm thick, 2.46  $\mu\text{m}$  wide BP sample assembled across four suspended Pd/Cr lines together with a schematic of the temperature profiles along the Pd/Cr heat line ( $i^{\text{th}}$  line) and one Pd/SiN<sub>x</sub> resistance thermometer line ( $j^{\text{th}}$  line,  $j \neq i$ ). (b) Tilted SEM image of a 39.2 nm thick BP flake displaying typical contact of a BP sample to a Pd/Cr line. Scale bars are 5  $\mu\text{m}$  for (a) and 1  $\mu\text{m}$  for (b).

Specifically, the temperature distribution in the  $j^{\text{th}}$  thermometer line that is not the  $i^{\text{th}}$  heating line as a function of position,  $x$ , as seen in Figure 2.2(a) is

$$\bar{\theta}_{j,i} = \frac{1}{2L_j} \int_{-L_j}^{L_j} \theta_{j,i}(x) dx, \text{ for } j \neq i \quad (2.4)$$

$$\bar{\theta}_{j,i} = \frac{1}{2L_j} \left[ \int_{-L_j}^{d_j-w_j} \frac{\theta_{c,j,i}(x+L_j)}{(d_j-w_j)+L_j} dx + \int_{d_j-w_j}^{d_j+w_j} \theta_{c,j,i} dx + \int_{d_j+w_j}^{L_j} \frac{\theta_{c,j,i}(x-L_j)}{(d_j+w_j)-L_j} dx \right] \quad (2.5)$$

Here,  $\bar{\theta}_{j,i}$  is the average temperature of the entire  $j^{\text{th}}$  line while heating the  $i^{\text{th}}$  line. Whereas,  $\theta_{c,j,i}$  is the temperature at the contact point in the  $j^{\text{th}}$  line i.e. the red plateau in Figure 2.2(a). Solving for the contact point temperature for the  $j^{\text{th}}$  thermometer line that is not the  $i^{\text{th}}$  heating line

$$\theta_{c,j,i} = \left( \frac{2L_j}{L_j+w_j} \right) \bar{\theta}_{j,i}, \text{ for } j \neq i, \quad (2.6)$$

where  $L_j$  and  $w_j$  are the half lengths and widths of the  $j^{\text{th}}$  line, respectively.

The thermal resistance of each of the four thermometer lines is

$$\frac{1}{R_{b,j}} = \frac{1}{\frac{L_j+(d_j-w_j)}{\kappa_j A_j}} + \frac{1}{\frac{L_j-(d_j+w_j)}{\kappa_j A_j}} \quad (2.7)$$

$$R_{b,j} = \frac{(L_j-w_j)^2 - d_j^2}{2\kappa_j A_j (L_j-w_j)} \quad (2.8)$$

where  $\kappa_j$ ,  $A_j$ , and  $d_j$  are the effective thermal conductivity, cross-sectional area, and displacement distance of the center of the flake to the center of the  $j^{\text{th}}$  suspended thermometer line.

The average temperature rise in the  $i^{\text{th}}$  heater line from Joule heating the  $i^{\text{th}}$  line as a function of position is

$$\bar{\theta}_{i,i} = \frac{1}{2L_i} \int_{-L_i}^{L_i} \theta_{i,i}(x) dx \quad (2.9)$$

$$\bar{\theta}_{i,i} = \frac{1}{2L_i} \left[ \int_{-L_i}^{d_i-w_i} \theta_{i,i,A}(x) dx + \int_{d_i-w_i}^{d_i+w_i} \theta_{c,i,i} dx + \int_{d_i-w_i}^{L_i} \theta_{i,i,B}(x) dx \right] \quad (2.10)$$

where  $\theta_{i,i,A}$  and  $\theta_{i,i,B}$  are functions of position describing the parabolic temperature profiles for each side of the plateau in Figure 2.2(a) and are defined as

$$\theta_{i,i,A}(x) = \frac{-(IV)_i}{4\kappa_i A_i L_i} x^2 + C_1 x + C_2 \quad (2.11)$$

$$C_1 = \frac{-(IV)_i}{4\kappa_i A_i L_i} [L_i - (d_i - w_i)] + \frac{\theta_{c,i,i}}{[L_i + (d_i - w_i)]} \quad (2.12)$$

$$C_2 = \frac{(IV)_i}{4\kappa_i A_i L_i} [L_i (d_i - w_i)] + \theta_{c,i,i} \left[ \frac{L_i}{L_i + (d_i - w_i)} \right] \quad (2.13)$$

$$\theta_{i,i,B}(x) = \frac{-(IV)_i}{4\kappa_i A_i L_i} x^2 + D_1 x + D_2 \quad (2.14)$$

$$D_1 = \frac{(IV)_i}{4\kappa_i A_i L_i} [L_i + (d_i + w_i)] - \frac{\theta_{c,i,i}}{[L_i - (d_i + w_i)]} \quad (2.15)$$

$$D_2 = \frac{-(IV)_i}{4\kappa_i A_i L_i} [L_i (d_i + w_i)] + \theta_{c,i,i} \left[ \frac{L_i}{L_i - (d_i + w_i)} \right] \quad (2.16)$$

Solving for the contact temperature as a function of Joule heating,  $(IV)_i$ , of the  $i^{th}$  Pd/Cr heating line

$$\theta_{c,i,i} = \left(\frac{2L_i}{L_i+w_i}\right) \bar{\theta}_{i,i} - \frac{1}{6} (IV)_i R_{b,i} \frac{[(L_i-w_i)^2(L_i^2-2L_iw_i+3d_i^2+w_i^2)]}{L_i(L_i+w_i)[(L_i-w_i)^2-d_i^2]} \quad (2.17)$$

An energy balance yields the following relationship

$$Q_{i,i} = -\sum_{\substack{j=1 \\ j \neq i}}^4 Q_{j,i} \quad (2.18)$$

$$Q_{j,i} = \frac{-\theta_{c,j,i}}{R_{b,j}}, \text{ for } j \neq i \quad (2.19)$$

Substituting and rearranging gives

$$\sum_{\substack{j=1 \\ j \neq i}}^4 \frac{\theta_{c,j,i}}{R_{b,j}} = -\kappa_i A_i \left. \frac{d\theta_{i,i,A}}{dx} \right|_{x=d_i-w_i} + \kappa_i A_i \left. \frac{d\theta_{i,i,B}}{dx} \right|_{x=d_i+w_i} + (IV)_i \frac{w_i}{L_i}, \text{ for } i = 1, 2, 3, 4 \quad (2.20)$$

Individually solving for the derivatives on the right hand side

$$\left. \frac{d\theta_{i,i,A}}{dx} \right|_{x=d_i-w_i} = \frac{-(IV)_i}{4\kappa_i A_i L_i} (L_i + d_i - w_i) + \frac{\theta_{c,i,i}}{L_i + d_i - w_i} \quad (2.21)$$

$$\left. \frac{d\theta_{i,i,B}}{dx} \right|_{x=d_i+w_i} = \frac{(IV)_i}{4\kappa_i A_i L_i} (L_i - d_i - w_i) - \frac{\theta_{c,i,i}}{L_i - d_i - w_i} \quad (2.22)$$

Plugging Equation (2.21) and (2.22) back into (2.20)

$$\sum_{\substack{j=1 \\ j \neq i}}^4 \frac{\theta_{c,j,i}}{R_{b,j}} = (IV)_i \frac{w_i}{L_i} + \kappa_i A_i \left[ \frac{(IV)_i}{4\kappa_i A_i L_i} 2(L_i - w_i) - \frac{\theta_{c,i,i}}{L_i + d_i - w_i} - \frac{\theta_{c,i,i}}{L_i - d_i - w_i} \right] \quad (2.23)$$

$$\sum_{\substack{j=1 \\ j \neq i}}^4 \frac{\theta_{c,j,i}}{R_{b,j}} = (IV)_i \frac{w_i}{L_i} + (IV)_i \left( \frac{L_i - w_i}{2L_i} \right) - \frac{k_i A_i}{L_i + d_i - w_i} \theta_{c,i,i} - \frac{k_i A_i}{L_i - d_i - w_i} \theta_{c,i,i} \quad (2.24)$$

$$\sum_{\substack{j=1 \\ j \neq i}}^4 \frac{\theta_{c,j,i}}{R_{b,j}} = (IV)_i \left( \frac{L_i + w_i}{2L_i} \right) - \frac{\theta_{c,i,i}}{R_{b,i}} \quad (2.25)$$

Substituting Equation (2.6) and (2.17) into (2.25) yields

$$\sum_{j=1}^4 \frac{1}{R_{b,j}} \frac{\bar{\theta}_{j,i}}{(IV)_i} \frac{2L_j}{L_j + w_j} = \frac{2[(L_i^3 - w_i^3)(L_i - w_i) - 3L_i d_i^2 w_i]}{3L_i(L_i + w_i)[(L_i - w_i)^2 - d_i^2]}, \text{ for } i = 1, 2, 3, 4 \quad (2.26)$$

This sum can be written in matrix form to solve for the thermal resistances of the four thermometer lines,  $R_{b,1}$ ,  $R_{b,2}$ ,  $R_{b,3}$ , and  $R_{b,4}$ , based on the 16 sets of  $\bar{\theta}_{j,i}/(IV)_i$  measurement data.

With the calculated  $R_{b,j}$  values, the contact point temperature rise for the  $i^{\text{th}}$  heater line of Equation (2.17) can be rewritten as

$$\theta_{c,i,i} = \theta_{i,i}(d_i - w_i < x < d_i + w_i) = R_{b,i} \left\{ (IV)_i \left( \frac{L_i + w_i}{2L_i} \right) - \sum_{\substack{j=1 \\ j \neq i}}^4 \left[ \frac{\bar{\theta}_{j,i}}{R_{b,j}} \left( \frac{2L_j}{L_j + w_j} \right) \right] \right\} \quad (2.27)$$

In the limit of vanishing width for all the above equations, the finite width derivation reverts to the contact point assumption, and the remainder of the four-probe thermal measurement solution follows the work of Kim et al. using relationships from the thermal circuit of Figure 2.1.

### 2.3 Sample Assembly

To maximize yield and throughput, the devices are fabricated utilizing conventional photolithography and etching techniques available at the Microelectronics Research Center. Eric Ou has detailed the four-probe device fabrication.<sup>59</sup> Four black phosphorus flakes were transferred to the four-probe microdevice. The measurement device for each sample had unique line length and resistance thermometer spacing, which is summarized in Table 2.1. The BP flakes had thicknesses of 39.2 nm, 55.6 nm, 145 nm, and 274 nm that were determined by either SEM or AFM. Raman spectroscopy confirmed that all flakes have the characteristic vibrational modes of BP. The nomenclature for the following material will drop the use of the descriptor “thick” to describe the dimension for the 39.2 nm, 55.6 nm, 145 nm, and 274 nm BP samples due to repetitiveness except for figure and table captions. Once successfully suspended across the four resistance thermometers, the crystal deterioration was minimized with the use of a high vacuum transport and storage apparatus consisting of a metal chamber connected to a butterfly valve.

BP Nanoribbon Thickness (nm)	Total Line Length ( $\mu\text{m}$ )	Gap 1-2 ( $\mu\text{m}$ )	Gap 2-3 ( $\mu\text{m}$ )	Gap 3-4 ( $\mu\text{m}$ )	Line Width ( $\mu\text{m}$ )
39.2	200	7	16	7	1.5
55.6	100	4	9	4	1.5
145	100	7	7	7	1.5
274	100	4	12	4	1.5

**Table 2.1.** Device dimensions for measured samples.

### **2.3.1 BP Exfoliation and Transfer**

Bulk BP flakes were obtained from a commercial source, Smart Elements. The bulk material was stored in a nitrogen desiccator to minimize hygroscopic degeneration and placed in a plastic container wrapped with aluminum foil to eliminate light interaction. To obtain few-layer black phosphorus, bulk BP was mechanically exfoliated using two Polydimethylsiloxane (PDMS) cubes each with a volume of approximately 1 cm<sup>3</sup>. Few-layer BP flakes exfoliated onto the PDMS surface can be seen with an optical microscope. Similar to SiO<sub>2</sub> oxide thickness corresponding to a specific color, an individual BP flake's color could be used to estimate thickness. The exfoliated BP flakes tended to separate along the AC and ZZ directions. The optical microscope is outfitted with a micromanipulator that uses a sharp tungsten probe to selectively transfer flakes. The PDMS surface is soft such that the probe tip can compress the surface and be positioned under the flake. Once under the flake, the probe is able to lift the flake off the surface, which sticks to the probe via van der Waals forces. The flake is then assembled onto a device where the resistance thermometer line spacing allows adequate maneuverability of the tungsten probe. This dry transfer process is expected to be cleaner compared to transfer techniques that utilize a Poly(methyl methacrylate) (PMMA) carrier layer.<sup>60</sup>

### **2.3.2 Sample Preparation**

A single 4" silicon wafer has a maximum yield of 2160 individual devices or 240 chips that are a 3 × 3 array of devices. A single chip measures 5 mm × 6 mm, and it is the maximum size that can fit in the chip carrier. The purpose of the chip carrier is to act as the

electric intermediary between the microscale device and the macroscale cryostat. Immediately following flake suspension on a device, the  $3 \times 3$  chip array is attached to a chip carrier using electrically conducting silver nanoparticle paint and stored inside a high vacuum transport apparatus to minimize degradation. The device is removed from the high vacuum apparatus, wire bonded to the chip carrier, and loaded into a temperature controlled cryostat. To eliminate convection, residual gas conduction, and radiation parasitic losses, the measurement is performed at a high vacuum of  $\sim 10^{-6}$  Torr with two radiation shields. In total, the flakes are exposed to atmosphere for thirty to ninety minutes during the assembly process of exfoliation, micromanipulator transfer, chip carrier attachment, wire bonding, and cryostat loading.

## **2.4 Measurement Process**

Thermal measurements of each sample were performed in the temperature range from 350 K to 10 K. High temperatures were avoided due to degradation concerns.<sup>61</sup> Low temperature measurements necessitated the use of liquid nitrogen from room temperature to 80 K and liquid helium from 80 K to 10 K. The low temperature measurements were necessary because the thermal conductivity peaks of BP occurred at 80 K for the 55.6 nm zigzag flake and 60 K for the other three armchair flake. Measurements below the peak temperature were performed to obtain additional data for the calculation of  $dR/dT$  for each suspended Pd/Cr line.

The thermal measurement is performed in the manner discussed in Section 2.1 using the finite width equations in Section 2.2. Further details of the four-probe thermal measurement are discussed by Eric Ou.<sup>59</sup> Because BP does not grow a native oxide, electrical contact to the resistance thermometer lines occurred for the 39.2 nm, 55.6 nm, and 145 nm samples. However, these electrical contacts were unstable resulting in no relevant electrical conductivity or Seebeck coefficient trends. BP samples with electrical contact to the resistance thermometer lines required the application of a floating current source for the heating line to separate the grounds of the  $i^{\text{th}}$  DC heating line and the  $j^{\text{th}}$  AC resistance thermometer. The 274 nm flake was in thermal contact resulting in the use of a heating current source with a common ground to the other measurement electronics. Multiple measurements are performed for each heating of the  $i^{\text{th}}$  line and measurement of the  $j^{\text{th}}$  line, and these measurements are averaged for the data analysis to minimize random uncertainty.

After thermal measurements were completed, the BP flakes were characterized with optical microscopy and scanning electron microscopy to obtain the flake dimensions that include the length of the middle suspended gap, width of the middle suspended sample, finite width of each BP contact to the resistance thermometer lines, and the displacement of each BP contact from the midpoint of their respective resistance thermometer line. Subsequently, the flakes were transferred with the micromanipulator from the measurement device onto a SiO<sub>2</sub> wafer piece with alignment marks. Atomic force

microscopy and polarized Raman spectroscopy were performed to obtain the nanoribbon thickness and crystallographic orientation.

## 2.5 Characterization Results

First, optical and scanning electron microscopes are used to visualize and measure the samples. Top-down SEMs of all four samples are shown in Figure 2.3. As thickness decreases, the BP transparency increases. The 274 nm flake in Figure 2.3(d) is completely opaque, and the flakes with thicknesses below 145 nm are partially transparent as seen in Figure 2.3(a-c). The 274 nm, 145 nm, and 55.6 nm flakes do not have any noticeable defects in contrast with the 39.2 nm flake.

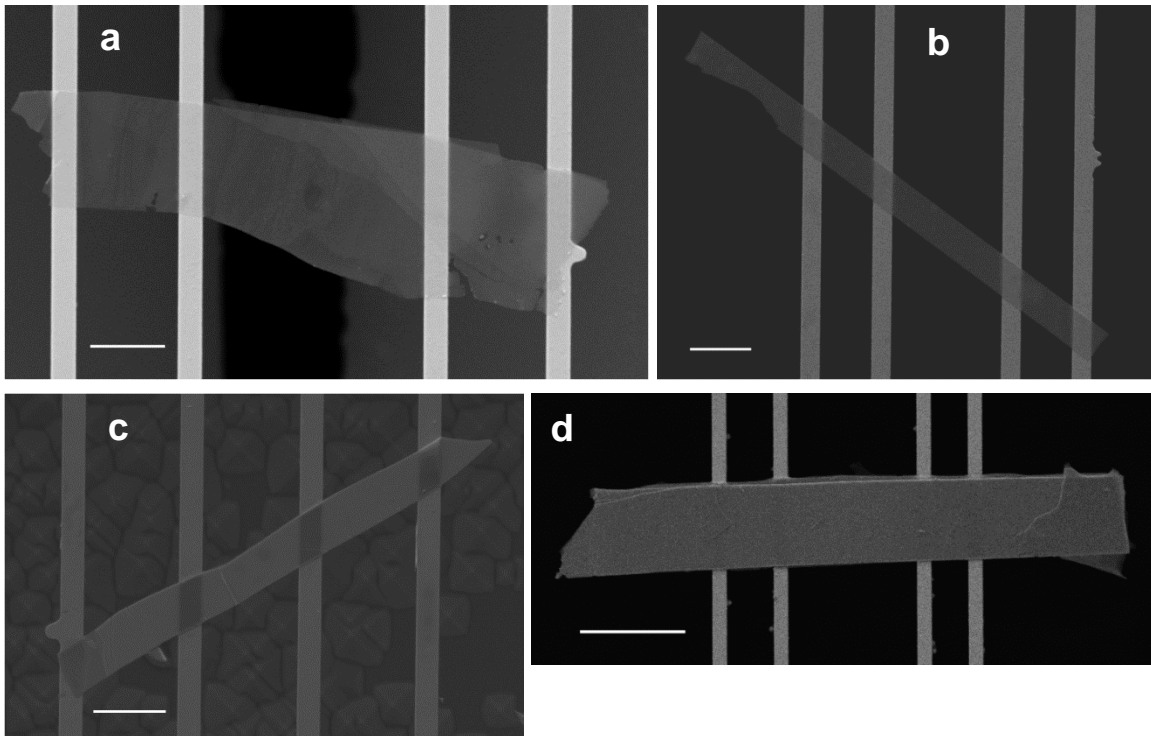


**Figure 2.3.** Top-down SEMs of measured BP flakes with thickness of (a) 39.2 nm, (b) 55.6 nm, (c) 145 nm, (d) 274 nm. Scale bar is 5  $\mu\text{m}$  (a-c) and 10  $\mu\text{m}$ .

Next, the flakes are transferred to a SiO<sub>2</sub>/Si wafer with alignment marks for atomic force microscopy and angle-resolved polarized Raman spectroscopy analysis. Figure 2.4 shows the AFM topographic height images obtained from normal tapping mode used to obtain sample thickness. Multiple thicknesses were obtained using the section function in the Nanoscope software package following the use of the 2<sup>nd</sup> order plane fit function to account for swiveling of the AFM probe. The section function lines are shown in Figure 2.4 along with topographic data in the corner. The thickness of the 274 nm sample was obtained from 85° tilted SEM analysis shown in Figure 2.5. The 274 nm, 145 nm, and 55.6 nm BP flakes have uniform width and thickness along the length of the middle suspended segment; however, the 39.2 nm flake has an irregular width and thickness along the middle suspended segment. Consequently, the width and thickness for the 39.2 nm BP sample are averaged to obtain the thermal conductivity. The samples display minimal topographic protrusions indicative of the BP degradation process.<sup>39</sup>

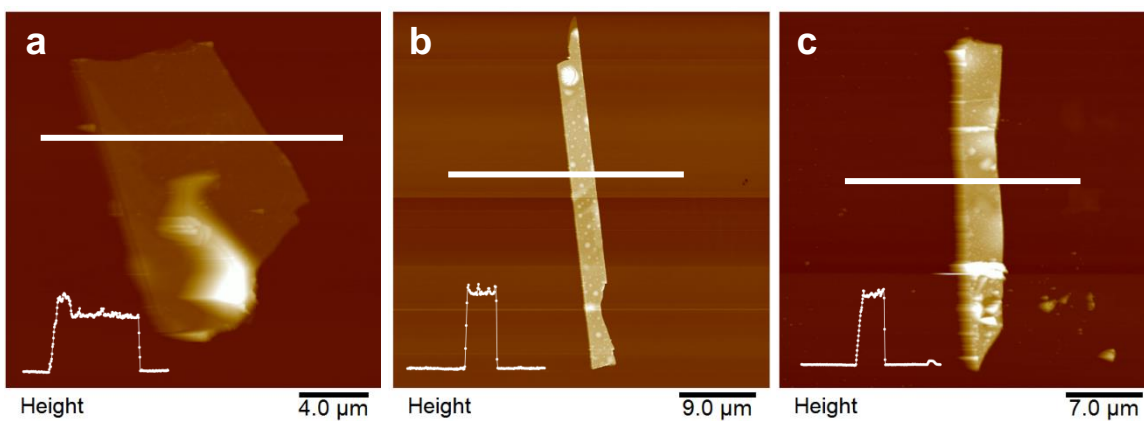


**Figure 2.4.** AFM height data used to obtain thicknesses of (a) 39.2 nm, (b) 55.6 nm, and (c) 145 nm via step function in the Nanoscope software package.

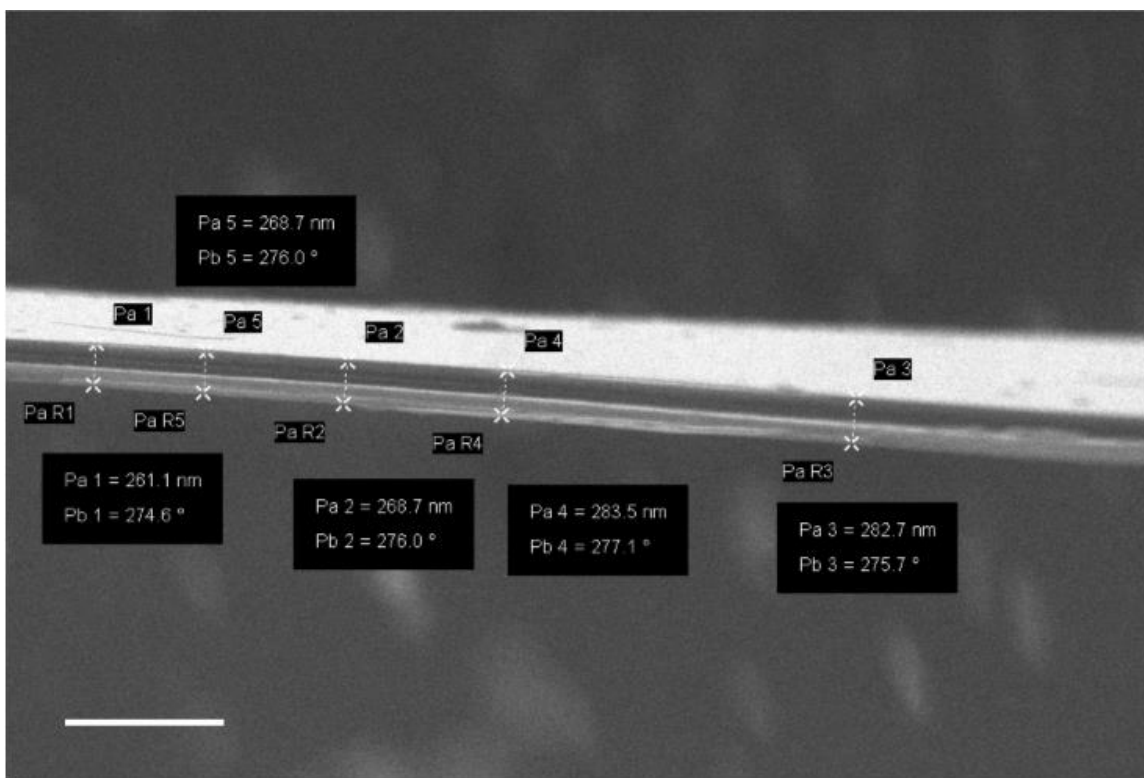


**Figure 2.5.** 85° tilted SEM of 274 nm thick BP flake used to obtain thickness in conjunction with other images. Scale bar is 1 μm.

Finally, angle-resolved polarized Raman spectroscopy was performed to obtain the lattice orientation of the flakes. Because the Raman apparatus had no rotational stage nor laser rotation capabilities, manual rotation of the flake about the sample normal in the  $a$ - $c$  plane was performed to obtain Raman versus orientation data. A 532 nm laser permanently polarized parallel to the  $x$ -axis was used to probe the  $A_g^1$ ,  $B_{2g}$ , and  $A_g^2$  black phosphorus vibrational modes where a typical response can be seen in Figure 2.6. Furthermore, as discussed in Section 1.1, the intensity ratio of the  $A_g^2$  peak to the  $A_g^1$  peak as a function of orientation can be used to determine the crystallographic direction of each sample. Figure 2.7 shows the  $A_g^2/A_g^1$  ratio versus the angle of the polarized laser for the 55.6 nm ZZ flake and the 39.2 nm AC flake. The 39.2 nm sample is oriented approximately  $22.5^\circ$  off the AC crystallographic direction with respect to the resistance thermometer lines of the measurement device. An armchair response was also observed for the 145 nm and 274 nm samples.

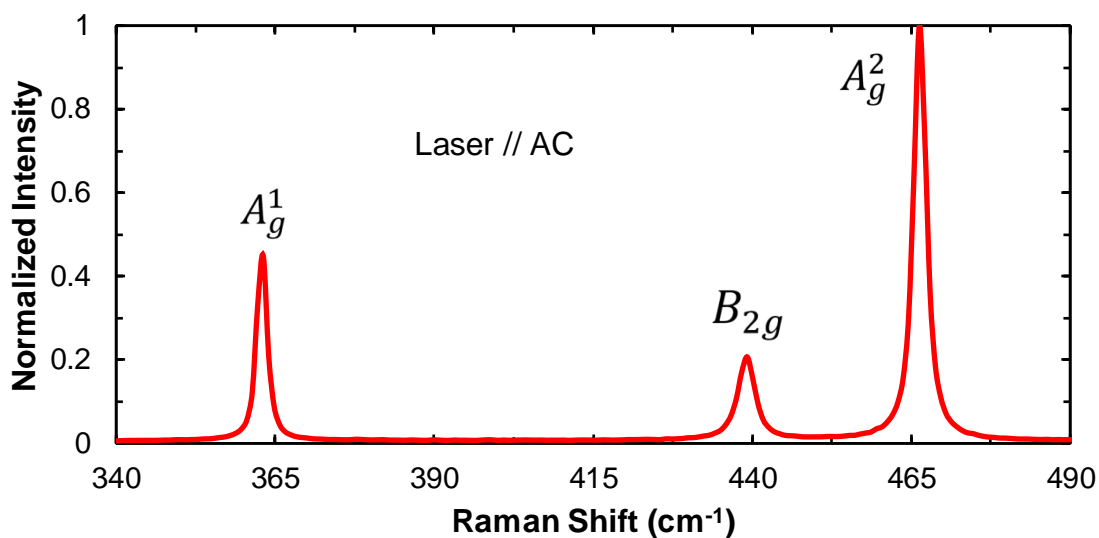


**Figure 2.6.** Typical Raman spectra for BP.

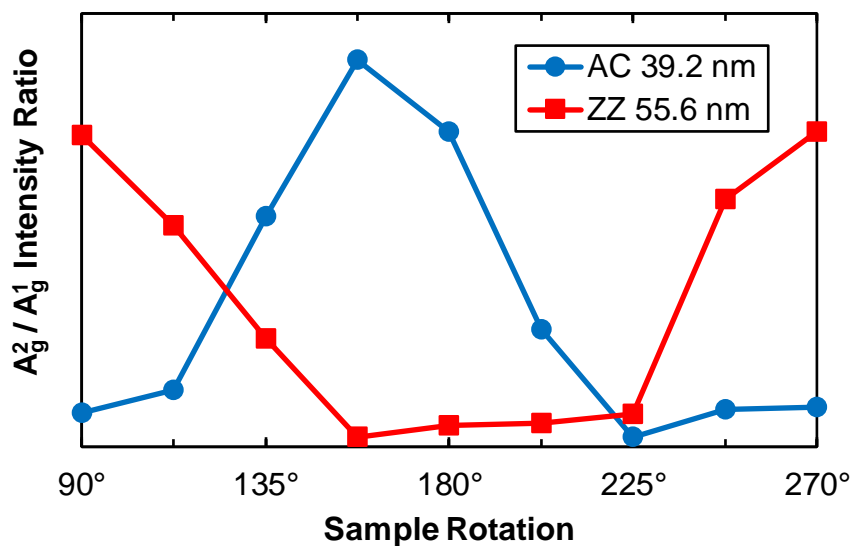


**Figure 2.7.** Angle-resolved polarized Raman spectra for two samples showing the lattice orientation dependence of the  $A_{2g}$  to  $A_{1g}$  intensity ratio. The lines are simple fitting to the measurement results (symbols). The rotation angles of  $90^\circ$  and  $180^\circ$  correspond to light polarization perpendicular and parallel, respectively, to the heat transport direction along the sample.

## 2.6 Uncertainty Analysis

Uncertainty analysis was performed to assess the confidence of the results by determining the accuracy and precision of the data. Error propagates throughout the measurement via random uncertainty in the measured sample dimensions and sample conductances.

Random and bias uncertainty of a variable  $X$  are the two components of total uncertainty that is defined as

$$\delta X_{Total} = \sqrt{\delta X_R^2 + \delta X_B^2} \quad (2.28)$$

where the subscripts  $R$  and  $B$  denote random and bias, respectively. Bias uncertainty is determined from the experimental instruments. Random uncertainty of a variable  $X$  is defined as

$$\delta X = \frac{\sigma_X}{\sqrt{N}} t \quad (2.29)$$

where  $\sigma_X$  is the standard deviation,  $N$  is the number of measurements, and  $t$  is the student  $t$ -distribution for a 95% confidence and a degree of freedom equal to one less than the number of measurements.

Multiple measurements of all sample dimensions were obtained from scanning electron microscopy and atomic force microscopy. Sample dimensions and their corresponding uncertainties are show in Table 2.2 where  $L$  is the length,  $w$  is the width, and  $t$  is the thickness.

BP Nanoribbon Thickness (nm)	$L$ ( $\mu\text{m}$ )	$\delta L$ ( $\mu\text{m}$ )	$w$ ( $\mu\text{m}$ )	$\delta w$ ( $\mu\text{m}$ )	$t$ (nm)	$\delta t$ (nm)
39.2	15.36	0.15	9.24	0.48	39.2	3.34
55.6	12.18	0.53	2.46	0.11	55.6	0.42
145	8.13	0.17	2.81	0.09	145	1.51
274	12.28	0.19	7.60	0.04	274	5.96

**Table 2.2.** Sample dimensions of the middle suspended segment and their uncertainty.

The error in the measured sample thermal conductivity in Figure 3.3 is derived from its definition, which is

$$\kappa = \frac{L}{R_2 A} \quad (2.30)$$

where  $L$  is the length,  $R_2$  is the intrinsic thermal resistance, and  $A$  is the cross sectional area equal to the multiplication of width and thickness. All variables are for the middle suspended segment of each sample. The total uncertainty for the thermal conductivity is defined as

$$\delta\kappa = \left[ \left( \frac{\partial\kappa}{\partial L} \delta L \right)^2 + \left( \frac{\partial\kappa}{\partial R_2} \delta R_2 \right)^2 + \left( \frac{\partial\kappa}{\partial w} \delta w \right)^2 + \left( \frac{\partial\kappa}{\partial t} \delta t \right)^2 \right]^{1/2} \quad (2.31)$$

$$\frac{\partial\kappa}{\partial L} = \frac{1}{R_2 w t} \quad (2.32)$$

$$\frac{\partial\kappa}{\partial R_2} = \frac{-L}{R_2^2 w t} \quad (2.33)$$

$$\frac{\partial\kappa}{\partial w} = \frac{-L}{R_2 w^2 t} \quad (2.34)$$

$$\frac{\partial \kappa}{\partial t} = \frac{-L}{R_2 w t^2} \quad (2.35)$$

Equation (2.1), (2.2), and (2.3) yield four values for each thermal resistance,  $R_2$ ,  $R_{c,2}$ ,  $R_{c,3}$ ,  $R_1+R_{c,1}$ , and  $R_3+R_{c,4}$ , using different subsets of the 16  $\bar{\theta}_{j,i}/(IV)_i$  measurement data. The range of each  $R_{thermal}$  uncertainty in Figure 3.2 is determined from the maximum and minimum of these four values. The beam resistance,  $R_{b,j}$ , uncertainty in Figure 3.1 are calculated from Equation (2.29). However, all 16  $\bar{\theta}_{j,i}/(IV)_i$  measurement data are used to obtain  $R_{b,1}$ ,  $R_{b,2}$ ,  $R_{b,3}$ , and  $R_{b,4}$  from Equation (2.26). Consequently, the different values needed for  $N$  and standard deviation are obtained by using individual  $\bar{\theta}_{j,i}/(IV)_i$  data as opposed to averaging the set of  $\bar{\theta}_{j,i}/(IV)_i$ .

Lastly, temperature error is incorporated into all conductivity and thermal resistance figures by plotting the average and range of variation. The average temperature is defined as

$$T_{Average} = T_{Cryostat} + \frac{\frac{\sum_{i=1}^4 \left( \frac{\theta_{c,2,i,max} + \theta_{c,3,i,max}}{2} \right)}{4}}{2} \quad (2.36)$$

where the subscript  $i$  denotes the heating line. The range minimum is the cryostat temperature while the range maximum is defined as

$$T_{MaximumError} = T_{Cryostat} + \text{MAX} \left[ \sum_{i=1}^4 \left( \frac{\theta_{c,2,i,max} + \theta_{c,3,i,max}}{2} \right) \right] \quad (2.37)$$

where  $MAX$  is an operator that extracts the maximum value from the summation.

## Chapter 3: Results and Discussion

### 3.1 Experimental Results

The thermal resistances of the thermal circuit in Figure 2.1 are analyzed first from the measurement data. Figure 3.1 shows the four beam thermal resistances  $R_{b,1}$ ,  $R_{b,2}$ ,  $R_{b,3}$ , and  $R_{b,4}$  as a function of temperature for the 145 nm BP flake. This is a typical Pd/Cr beam resistance response for all measured devices where  $R_{b,j}$  is defined in Equation (2.8). In metals, the electronic contribution dominates the total thermal conductivity and increases with temperature. Referring to Table 2.1, the devices for measuring the 55.6 nm and 274 nm flakes have beam resistances with the same magnitude as the device for measuring the 145 nm flake because their total beam lengths are the same. Conversely, the device for measuring the 39.2 nm flake has double the total beam length, and the magnitude of  $R_{b,j}$  is approximately two fold greater than the 145 nm flake beam resistances.

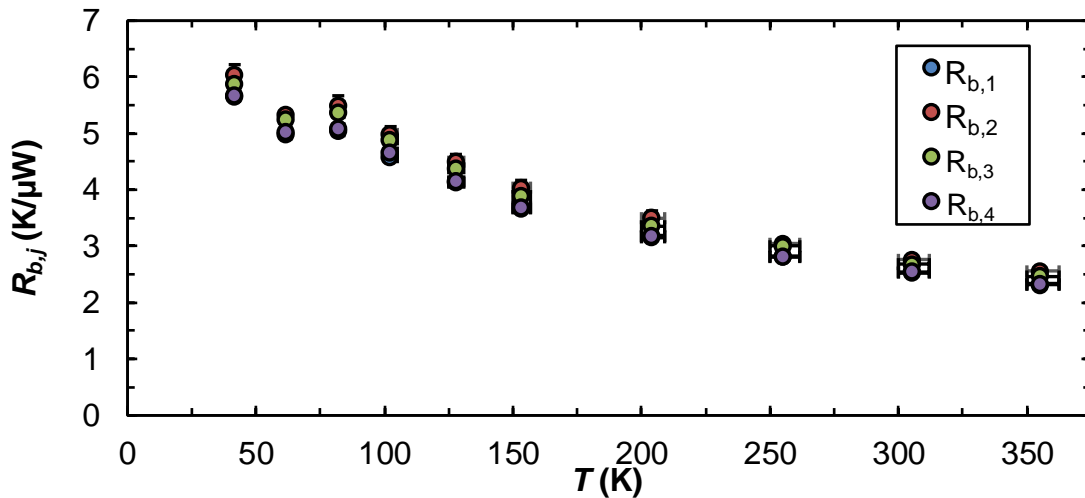


**Figure 3.1.** Pd/Cr line thermal resistance as a function of temperature for 145 nm thick BP sample. The error bars of some of the data are smaller than the symbol size.

Continuing the discussion on the resistances of the thermal circuit, Figure 3.2(a-d) shows  $R_2$ ,  $R_{c,2}$ ,  $R_{c,3}$ ,  $R_1+R_{c,1}$ , and  $R_3+R_{c,4}$  as a function of temperature for each BP flake. The 39.2 nm sample in Figure 3.2(a) shows an abrupt change in contact resistance at beam four between measurements at 100 K and 125 K for  $R_3+R_{c,4}$ , which does not affect the measurement of  $R_2$ . Figure 2.2(b) shows the BP flake contact to the fourth beam for the 39.2 nm sample. Similarly for the 274 nm BP flake,  $R_{c,1}$  increases noticeably below 150 K in Figure 3.2(d) suggesting poor contact to the Pd/SiN<sub>x</sub> resistance thermometer.

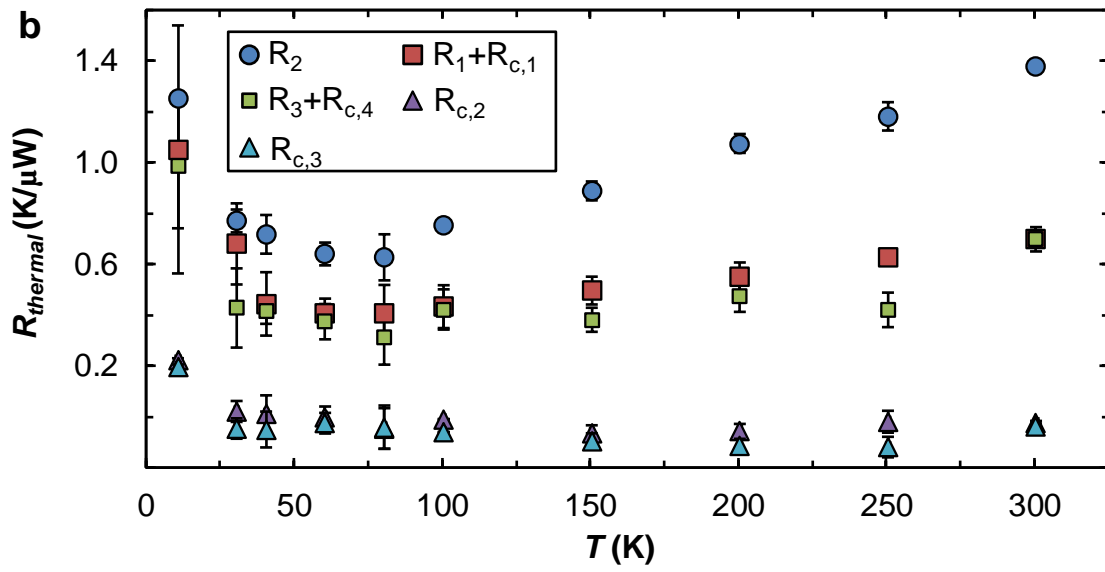
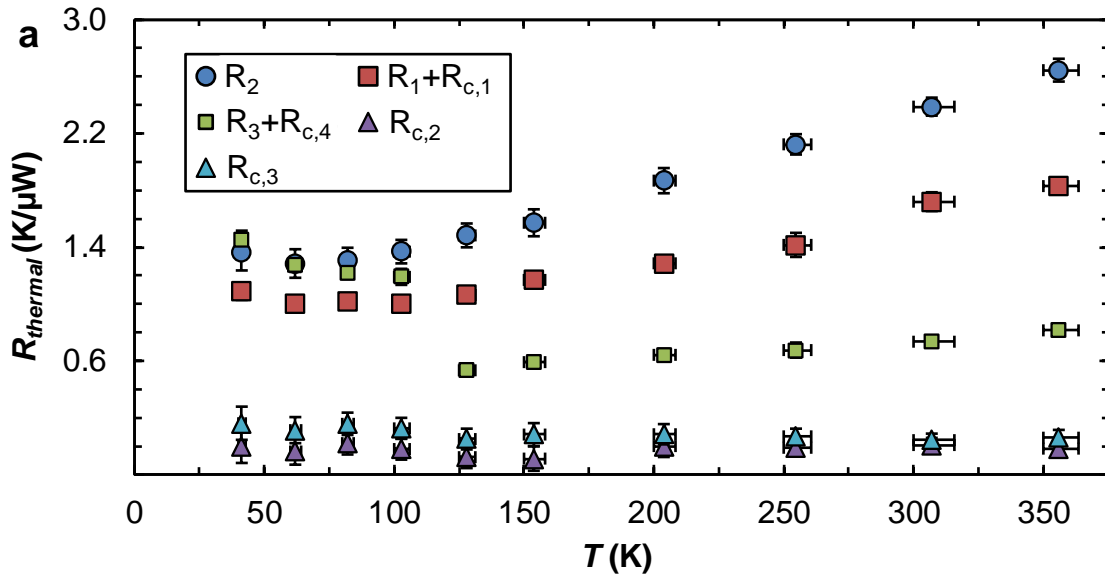
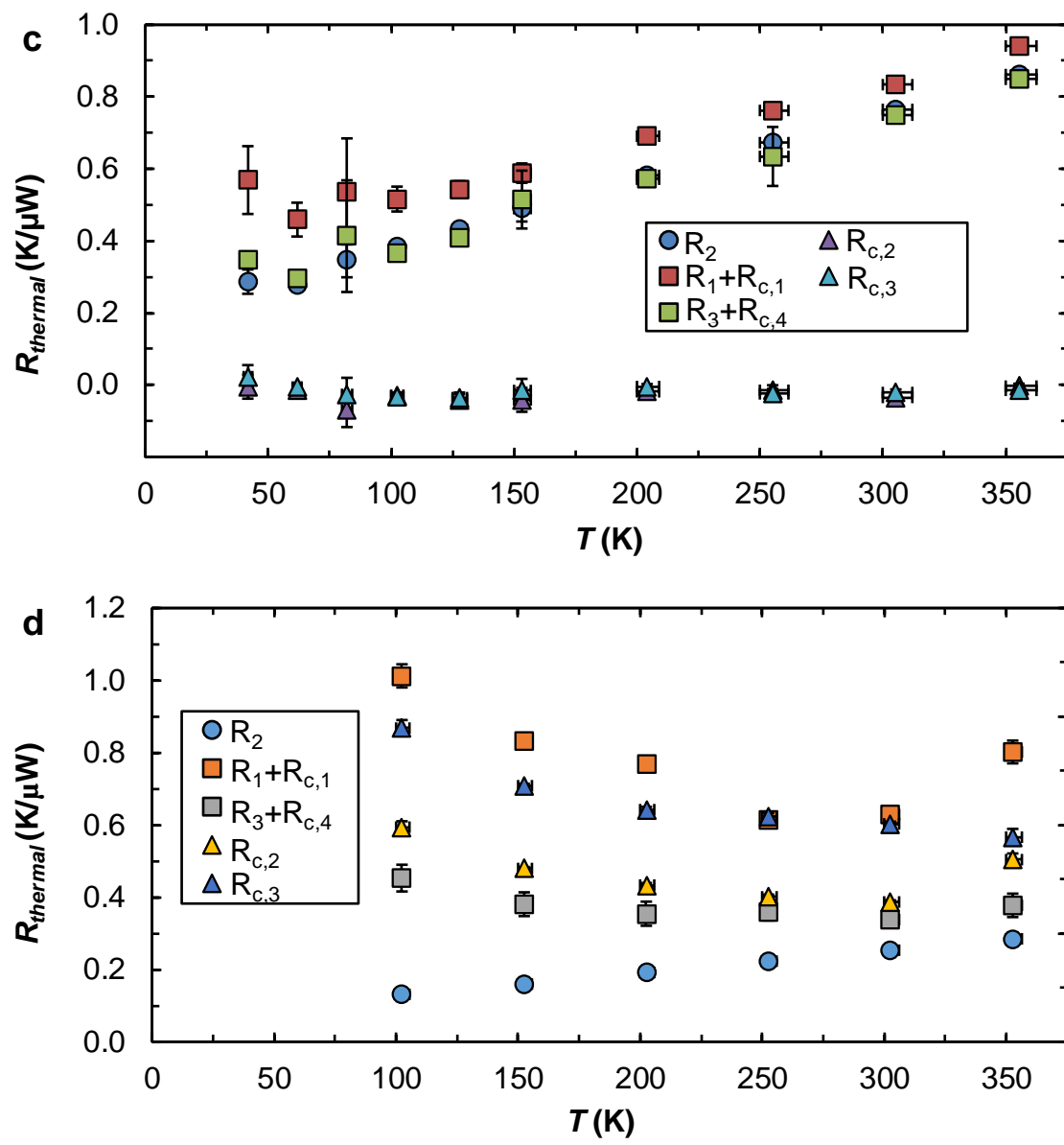


Figure 3.2 is continued on the next page.



**Figure 3.2.** Thermal resistances as a function of temperature for (a) 39.2 nm, (b) 55.6 nm, (c) 145 nm, and (d) 274 nm thick BP samples. The error bars of some of the data are smaller than the symbol size.

BP Nanoribbon Thickness (nm)	$R_{c,2}$ Average (K/ $\mu$ W)	$R_{c,2}$ High (K/ $\mu$ W)	$R_{c,2}$ Low (K/ $\mu$ W)	$R_{c,3}$ Average (K/ $\mu$ W)	$R_{c,3}$ High (K/ $\mu$ W)	$R_{c,3}$ Low (K/ $\mu$ W)
39.2	-0.023	0.021	-0.088	0.094	0.161	0.042
55.6	0.004	0.221	-0.063	-0.039	0.197	-0.119
145	-0.027	-0.003	-0.069	-0.016	0.023	-0.035

**Table 3.1.** Average, high, and low contact resistance values for the two middle beams for the 39.2 nm, 55.6 nm, and 145 nm thick BP flakes.

The contact resistance at beam two,  $R_{c,2}$ , and three,  $R_{c,3}$ , are too small and too close to zero to be measured for the 39.2 nm, 55.6 nm, and 145 nm samples at certain temperatures. This outcome is a result of measurement sensitivity and uncertainty. Similar to an earlier two-probe thermal measurement, the noise and resolution of the four-probe thermal measurement is constrained by a 10–50 mK temperature fluctuation of the cryostat sample stage.<sup>62</sup> The temperature volatility of the microdevice affects the measurement of the beam thermal resistances that are used to calculate the heat flow rates into the sample at the contact points, which is then used to calculate the contact resistances. The smallest measurable contact resistance is approximately a 100<sup>th</sup> of  $R_b$ .<sup>62</sup> Because the 55.6 nm and 145 nm BP flakes have a total beam length of 100  $\mu$ m and the 39.2 nm BP flake has a total beam length of 200  $\mu$ m, the minimum sensitivity is about 0.06 K/ $\mu$ W and 0.11 K/ $\mu$ W, respectively. Table 3.1 summarizes the average, high, and low values of contact resistance for beams two and three for the flakes with negative contact resistance values. The negative contact resistance values are comparable to the sensitivity of the measurement. Hence, the interfacial contact between the BP and Pd/SiN<sub>x</sub> is good such that the thermal resistance is

below the sensitivity of the measurement where the negative values are a result of noise and uncertainty.

### 3.2 Temperature and Thickness Dependence

The thermal conductivity of the four BP flakes are shown in Figure 3.3 elucidating the distinct anisotropy along the zigzag and armchair in-plane directions, which agrees with theoretical predictions and experimental measurements.<sup>24,29–36</sup> In particular, the thermal conductivity along the zigzag high-symmetry direction is threefold higher than the armchair samples, which was predicted in theoretical works.<sup>24,29–32</sup> Low temperature thermal conductivity peaks for each sample were also observed. The thermal conductivity peak arises from the reduction of the umklapp process and increased importance of geometrical effects and imperfections. These two phenomena are best understood with the mathematical definition of lattice thermal conductivity,  $\kappa$ , that is defined as<sup>63</sup>

$$\kappa = \sum_{\mathbf{k}} C_{\mathbf{k}} (v_{\mathbf{k}} \cdot \hat{t})^2 \tau_{\mathbf{k}} \quad (3.1)$$

where  $C_{\mathbf{k}}$  is the specific heat supplied by the mode with the wavevector  $\mathbf{k}$ ,  $v$  is the phonon group velocity,  $\hat{t}$  is the unit vector in the direction of temperature gradient,  $\tau$  is the phonon relaxation time following Matthiessen's rule, and the summation is over the first Brillouin zone of all wavevector modes. The decrease in thermal conductivity at low temperatures is caused by imperfections and geometrical or size effects, which encompasses phonon scattering by crystal boundaries, chemical impurities, lattice imperfections, etc.<sup>64</sup> Crystal imperfections and size effects reduce the phonon relaxation time. Alternatively, umklapp

scattering, primarily phonon–phonon scattering between the optical and acoustic branches, diminishes at low temperatures because high energy optical modes become frozen or inactive. Thus, the acoustic phonons scatter less, which causes an increase in the relaxation time. The temperature at which a crystal’s thermal conductivity reaches its maximum occurs lower for crystals with less imperfections, *ceteris paribus*.

Observing the temperature dependence of the 39.2 nm and 145 nm samples, the difference in thermal conductivities becomes greater at decreasing temperature. This may be due to extrinsic scattering such as boundary scattering, which has a more pronounced effect at low temperatures than at high temperatures, or crystal imperfections that influences the phonon relaxation time. The thermal conductivity separation for decreasing temperature between the 274 nm and 145 nm flakes is miniscule compared to the 39.2 nm and 145 nm flakes. This result suggest that imperfections such as point defects are more important than boundary scattering in the temperature range below the thermal conductivity peak. Figure 2.3(a) shows stacking defects, holes, and tears for the 39.2 nm sample that do not exist in either the 145 nm or 274 nm samples. Another trend is that increasing temperature causes decreasing thermal conductivity for all samples, which is expected for a crystalline material with phonon-dominated heat transport, indicating that phonon-phonon scattering dominates as opposed to extrinsic scattering.

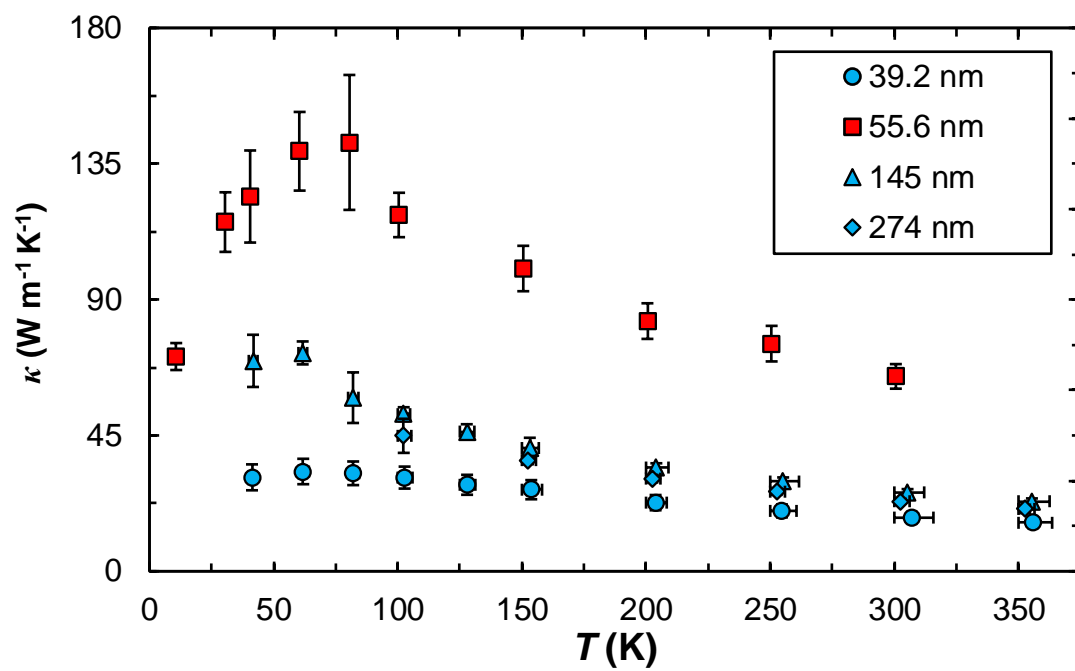


**Figure 3.3.** In-plane thermal conductivity of suspended few-layer black phosphorus for samples oriented along the AC (blue) and ZZ (red) direction. The error bars of some of the data are smaller than the symbol size.

This work's thermal conductivities are compared against previous experimental studies in Figure 3.4 and Figure 3.5.<sup>33-35</sup> The thermal conductivity results utilizing TR-MOKE were not included in the figures because Zhu et al. measured bulk BP flakes on the order of tens of microns.<sup>36</sup> In addition to the experimental results, Bjorn Vermeersch, Jesús Carrete, and Natalio Mingo are collaborators who have provided thermal conductivity first principles calculations seen as the dashed and solid lines in the aforementioned figures. The dashed lines represent pristine, defect-free thermal conductivities while the solid lines represent thermal conductivities with vacancy defects. The vacancy defects are imperfections in the crystal that scatter phonons decreasing the phonon relaxation time and crystal thermal conductivity. For the four-probe samples, the vacancy point defect concentrations are 0.04%, 0.145%, 0.1%, and 0.14%, respectively for the 55.6 nm, 274 nm, 145 nm, and 39.2 nm samples. The first principles calculation technique to obtain thermal conductivity is described in detail in a previous publication by the collaborators.<sup>65</sup> Briefly, the calculations were performed using VASP with projector-augmented-wave datasets.<sup>66,67</sup> A generalized Fuchs model was then employed to obtain the thermal conductivity while accounting for the BP anisotropy for the defect-free results. Vacancy defects were modeled as mass defects with an effective mass equal to three times the mass of a phosphorus atom. Three-dimensional Monte Carlo simulations were used to extract thermal conductivity for the vacancy defect results.

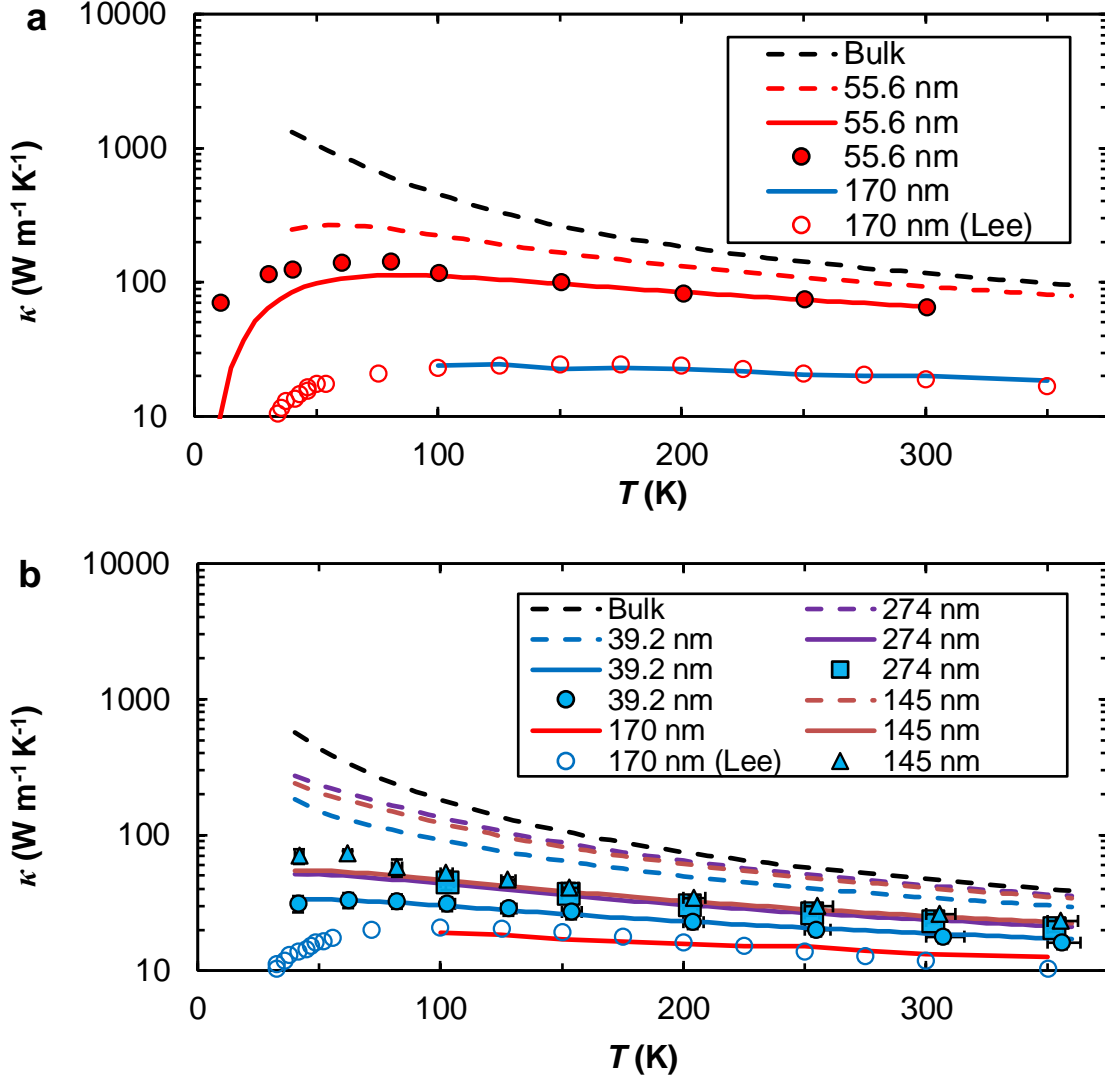


**Figure 3.4.** Temperature dependence of the basal-plane thermal conductivities of the BP samples measured in this work (filled symbols) and in a recent report by Lee et al.<sup>34</sup> (unfilled symbols) for the zigzag (a) and the armchair (b) directions. The dashed lines are the theoretical calculation results for defect-free samples. The solid lines are the calculation results with additional phonon scattering by vacancy point defects at a concentration of 0.04%, 0.145%, 0.1%, and 0.14%, respectively for the 55.6 nm, 274 nm, 145 nm, and 39.2 nm samples, 0.6% and 0.4 % for the 170 nm thick, zigzag-oriented and armchair-oriented samples of Lee et al.,<sup>34</sup> respectively. The dashed and solid lines are provided by collaborators Bjorn Vermeersch, Jesús Carrete, and Natalio Mingo. The sample thickness is indicated in the legend. The error bars of some of the data from this work are smaller than the symbol size.

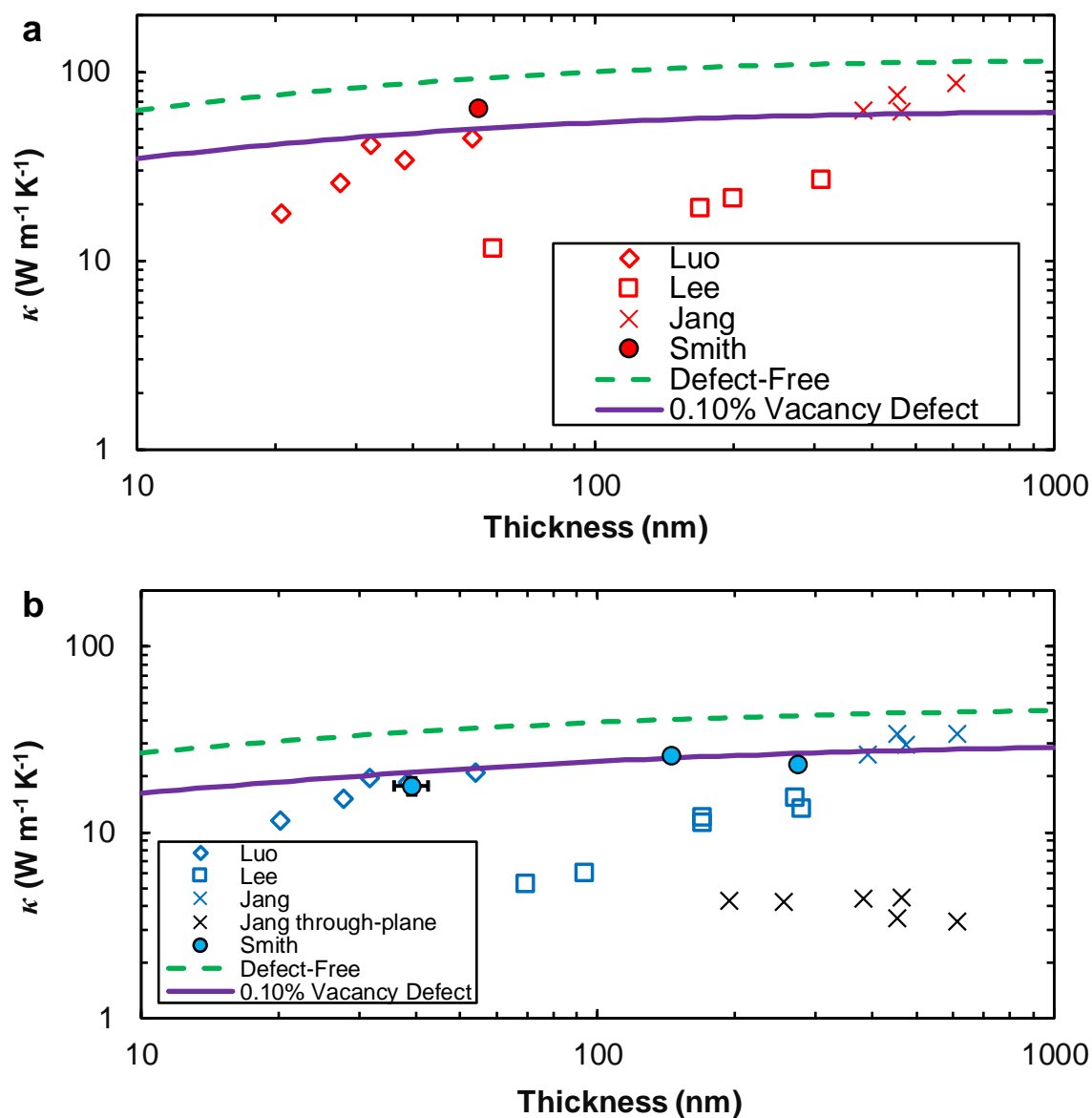


**Figure 3.5.** Thickness dependence of the room-temperature thermal conductivities of the BP samples measured in this work (filled circles), by Luo et al.<sup>33</sup> with micro-Raman thermometry (unfilled diamond symbols), by Lee et al.<sup>34</sup> with a two-probe method (unfilled square symbols), and by Jang et al.<sup>35</sup> using TDTR (crosses) for the zigzag (a, red symbols) direction and the armchair (b, blue symbols) and through-plane direction (b, black crosses) directions. The dashed and solid lines are the calculation results for defect-free samples and samples with 0.1% point vacancies, respectively, provided by collaborators Bjorn Vermeersch, Jesús Carrete, and Natalio Mingo.

Figure 3.4 shows the temperature dependence of thermal conductivity for different BP thicknesses comparing the two-probe microdevice utilized by Lee et al.<sup>34</sup> (unfilled symbols) and this work's four-probe microdevice (filled symbols). In agreement with theoretical predictions, both measurement methods have obtained higher thermal conductivities along the ZZ direction than along the AC direction.<sup>24,30-32</sup> Nevertheless, the four-probe measurements have produced higher thermal conductivity values for both in-plane, high symmetry directions across the entire temperature range. Similar to Lee et al., the thermal conductivity of the armchair orientated flakes peak at a lower temperature than the zigzag oriented flake. However, the temperature of the peak location is different between the two-probe and four-probe microdevices. The AC samples peak at ~60 K and the ZZ sample peaks at ~80 K compared to Lee et al.'s ~100 K and ~150 K for AC and ZZ, respectively.

It is noted that in the two-probe measurements reactive ion etching was utilized to pattern their samples to a width of 540–590 nm, which is much smaller than the 2.46–9.24  $\mu\text{m}$  widths of the exfoliated samples used for the four-probe measurements without etching. This work's higher thermal conductivity and location of the thermal conductivity low-temperature peaks compared to Lee et al.<sup>34</sup> provide insight into fabrication processes that can damage the suspended sample and reveal the importance of extrinsic scattering. Lee et al. obtains BP nanoribbons via a top-down microfabrication process that involves two spin coats of PMMA, reactive ion etching, and argon ion milling. These microfabrication steps employed by Lee et al. have the possibility of physically damaging

the sample thereby creating point defects and increasing the scattering site density.<sup>60,68–71</sup> In contrast, this work employs no microfabrication techniques utilized by Lee and his colleagues.

Referring to Equation (3.1), the relaxation time is lowered due to phonon scattering off size effects or imperfections, which explains the low thermal conductivity values reported by Lee et al. using a two-probe microdevice. Additionally, an increase in the imperfection concentration explains why Lee et al.'s thermal conductivity peaks occur at a higher temperature where scattering off imperfections limits the thermal conductivity at low temperatures. This is confirmed by the collaborators who fit the temperature-dependent thermal conductivity curves by adding vacancy defects. The 170 nm Lee et al. curves have approximately 0.6% and 0.4% vacancy defect concentration for their ZZ and AC samples, respectively. This imperfection concentration is much larger than the four-probe samples. Hence, the high thermal conductivity of the 55.6 nm sample is due to having less crystal imperfections.

Figure 3.5 shows the thickness dependence of thermal conductivity for both crystallographic directions at room-temperature for three measurement techniques discussed in Section 1.1.1. In addition, a defect-free dashed curve and a 0.1% vacancy defect concentration solid curve is plotted from collaborator data. The room-temperature thermal conductivity magnitudes of the four-probe measured samples are comparable to those reported from the micro-Raman thermometry measurement<sup>33</sup> and TDTR

measurement.<sup>35</sup> These two techniques have only obtained the near-room-temperature values. The values obtained for the four-probe samples are lower than the values measured by the TDTR technique in much thicker flakes.<sup>35</sup> The 55.6 nm ZZ-oriented sample measured in this work exhibits the highest thermal conductivity of  $142 \pm 22 \text{ W m}^{-1} \text{ K}^{-1}$  at 80 K and a value of  $65 \pm 4 \text{ W m}^{-1} \text{ K}^{-1}$  at room temperature. This sample has higher thermal conductivity than reported values for MoS<sub>2</sub>.<sup>46,51,72</sup>

There is a pronounced thermal conductivity thickness dependence of sub-100 nm BP flake samples measured by the micro-Raman technique. However, the first principles calculations by the collaborators, which is confirmed by the AC four-probe results, suggests a less sensitive thickness-dependence of thermal conductivity highlighting the phonon focusing effect. The phonon focusing effect is the result of minimal phonon scattering off bottom and top layers in thin 2D layers compared to thin films of a relatively isotropic structure, as discussed in an earlier work on thin MoS<sub>2</sub>.<sup>51</sup> Due to less phonon scattering off top and bottom layers, the thermal conductivity does not depend as strongly on thickness. Comparing the results of the micro-Raman and TDTR measurements to the 0.1% vacancy defect concentration line, micro-Raman thinner samples require a much higher point defect concentration while fitting the TDTR samples require a point defect concentration lower than 0.1%. It is important to note again that the micro-Raman samples are exposed to flowing nitrogen gas while the TDTR samples are capped in an aluminum oxide layer. In addition, the two-probe samples underwent etching processes unlike the four-probe samples but each were measured in vacuum. The differences in sample

preparation and measurement between the four measurement techniques reveal the importance of BP surface degradation, which results in higher concentration of point defects.

## Chapter 4: Conclusion

The intrinsic in-plane thermal conductivity of few-layer black phosphorus has been measured in this work. Development of a four-probe finite width solution was derived necessitated by the width of the exfoliated BP flakes and their high thermal conductivity. Four BP samples were measured and subsequently characterized to determine sample dimensions and the crystallographic orientation. The extracted intrinsic thermal conductivity was anisotropic with the zigzag direction having threefold thermal conductivity than the armchair direction. The largest intrinsic thermal conductivity of  $142 \text{ W m}^{-1} \text{ K}^{-1}$  at 80 K and a value of  $65 \text{ W m}^{-1} \text{ K}^{-1}$  at room temperature was obtained from a 55.6 nm thick zigzag-oriented sample at 80 K. The contact resistance was determined to be smaller than the sensitivity of the measurement, which is limited by the magnitude of the suspended Pd/SiN<sub>x</sub> beam resistances.

The thermal conductivity magnitudes obtained from the four-probe thermal transport measurement of black phosphorus agreed with results from micro-Raman thermometry and TDTR. However, the collaboration results and AC four-probe data show a less sensitive thickness-dependence of thermal conductivity than the pronounced sub-100 nm dependence by micro-Raman thermometry measurement. The weak thermal conductivity dependence on thickness is attributed to the phonon focusing effect. In addition, this work's four-probe measurement results compared to results from a two-probe microdevice measurement were dissimilar, which can be explained from extrinsic scattering e.g. point defects caused by microfabrication techniques. This work has shown

the weak thermal conductivity thickness dependence of BP as well as the room for improvement of BP thermal conductivity by reducing defects. These results provide insight for thermal management design and fabrication of 2D nanomaterial logic systems especially flexible electronic devices.

## References

- (1) Moore, G. E. Cramming More Components onto Integrated Circuits. *Proc. IEEE* **1998**, *86*, 82–85.
- (2) Schelling, P. K.; Shi, L.; Goodson, K. E. Managing Heat for Electronics. *Mater. Today* **2005**, *8*, 30–35.
- (3) Moore, A. L.; Shi, L. Emerging Challenges and Materials for Thermal Management of Electronics. *Mater. Today* **2014**, *17*, 163–174.
- (4) Akinwande, D.; Petrone, N.; Hone, J. Two-Dimensional Flexible Nanoelectronics. *Nat. Commun.* **2014**, *5*, 5678.
- (5) Chang, H. Y.; Yang, S.; Lee, J.; Tao, L.; Hwang, W. S.; Jena, D.; Lu, N.; Akinwande, D. High-Performance, Highly Bendable MoS<sub>2</sub> Transistors with High-K Dielectrics for Flexible Low-Power Systems. *ACS Nano* **2013**, *7*, 5446–5452.
- (6) Lee, G.-H.; Yu, Y.-J.; Cui, X.; Petrone, N.; Lee, C.-H.; Choi, M. S.; Lee, D.-Y.; Lee, C.; Yoo, W. J.; Watanabe, K.; *et al.* Flexible and Transparent MoS<sub>2</sub> Field-Effect Transistors on Hexagonal Boron Nitride-Graphene Heterostructures. *ACS Nano* **2013**, *7*, 7931–7936.
- (7) Lee, J.; Ha, T. J.; Li, H.; Parrish, K. N.; Holt, M.; Dodabalapur, A.; Ruoff, R. S.; Akinwande, D. 25 GHz Embedded-Gate Graphene Transistors with High-K Dielectrics on Extremely Flexible Plastic Sheets. *ACS Nano* **2013**, *7*, 7744–7750.

- (8) Das, S.; Gulotty, R.; Sumant, A. V.; Roelofs, A. All Two-Dimensional, Flexible, Transparent, and Thinnest Thin Film Transistor. *Nano Lett.* **2014**, *14*, 2861–2866.
- (9) Lee, C.; Wei, X.; Kysar, J. W.; Hone, J. Measurement of the Elastic Properties and Intrinsic Strength of Monolayer Graphene. *Science* **2008**, *321*, 385–388.
- (10) Sadeghi, M. M.; Park, S.; Huang, Y.; Akinwande, D.; Yao, Z.; Murthy, J.; Shi, L. Quantitative Scanning Thermal Microscopy of Graphene Devices on Flexible Polyimide Substrates. *J. Appl. Phys.* **2016**, *119*, 235101.
- (11) Novoselov, K. S.; Geim, A. K.; Morozov, S. V.; Jiang, D.; Zhang, Y.; Dubonos, S. V.; Grigorieva, I. V.; Firsov, A. A. Electric Field Effect in Atomically Thin Carbon Films. *Science (80-. )*. **2004**, *306*, 666–669.
- (12) Chen, J. R.; Odenthal, P. M.; Swartz, A. G.; Floyd, G. C.; Wen, H.; Luo, K. Y.; Kawakami, R. K. Control of Schottky Barriers in Single Layer MoS<sub>2</sub> Transistors with Ferromagnetic Contacts. *Nano Lett.* **2013**, *13*, 3106–3110.
- (13) Fang, H.; Chuang, S.; Chang, T. C.; Takei, K.; Takahashi, T.; Javey, A. High-Performance Single Layered WSe<sub>2</sub> P-FETs with Chemically Doped Contacts. *Nano Lett.* **2012**, *12*, 3788–3792.
- (14) Watanabe, K.; Taniguchi, T.; Kanda, H. Direct-Bandgap Properties and Evidence for Ultraviolet Lasing of Hexagonal Boron Nitride Single Crystal. *Nat. Mater.* **2004**, *3*, 404–409.

- (15) Meric, I.; Dean, C. R.; Petrone, N.; Wang, L.; Hone, J.; Kim, P.; Shepard, K. L. Graphene Field-Effect Transistors Based on Boron-Nitride Dielectrics. *Proc. IEEE* **2013**, *101*, 1609–1619.
- (16) Vogt, P.; De Padova, P.; Quaresima, C.; Avila, J.; Frantzeskakis, E.; Asensio, M. C.; Resta, A.; Ealet, B.; Le Lay, G. Silicene: Compelling Experimental Evidence for Graphenelike Two-Dimensional Silicon. *Phys. Rev. Lett.* **2012**, *108*, 1–5.
- (17) Davila, M. E.; Xian, L.; Cahangirov, S.; Rubio, A.; Le Lay, G. Germanene: A Novel Two-Dimensional Germanium Allotrope Akin to Graphene and Silicene. *New J. Phys.* **2014**, *16*.
- (18) Li, L.; Yu, Y.; Ye, G. J.; Ge, Q.; Ou, X.; Wu, H.; Feng, D.; Chen, X. H.; Zhang, Y. Black Phosphorus Field-Effect Transistors. *Nat. Nanotechnol.* **2014**, *9*, 372.
- (19) Liu, H.; Neal, A. T.; Zhu, Z.; Luo, Z.; Xu, X.; Tománek, D.; Ye, P. D. Phosphorene: An Unexplored 2D Semiconductor with a High Hole Mobility. *ACS Nano* **2014**, *8*, 4033–4041.
- (20) Xia, F.; Wang, H.; Jia, Y. Rediscovering Black Phosphorus as an Anisotropic Layered Material for Optoelectronics and Electronics. *Nat. Commun.* **2014**, *5*, 4458.
- (21) Koenig, S. P.; Doganov, R. A.; Schmidt, H.; Castro Neto, A. H.; Özyilmaz, B. Electric Field Effect in Ultrathin Black Phosphorus. *Appl. Phys. Lett.* **2014**, *104*, 103106.

- (22) Zhu, W.; Yogeesh, M. N.; Yang, S.; Aldave, S. H.; Kim, J.-S.; Sonde, S.; Tao, L.; Lu, N.; Akinwande, D. Flexible Black Phosphorus Ambipolar Transistors, Circuits and AM Demodulator. *Nano Lett.* **2015**, *15*, 1883–1890.
- (23) Butler, S. Z.; Hollen, S. M.; Cao, L.; Cui, Y.; Gupta, J. A.; Gutiérrez, H. R.; Heinz, T. F.; Hong, S. S.; Huang, J.; Ismach, A. F.; *et al.* Opportunities in Two-Dimensional Materials Beyond Graphene. *ACS Nano* **2013**, *7*, 2898–2926.
- (24) Fei, R.; Faghaninia, A.; Soklaski, R.; Yan, J. A.; Lo, C.; Yang, L. Enhanced Thermoelectric Efficiency via Orthogonal Electrical and Thermal Conductances in Phosphorene. *Nano Lett* **2014**, *14*, 6393–6399.
- (25) Wei, Q.; Peng, X. Superior Mechanical Flexibility of Phosphorene and Few-Layer Black Phosphorus. *Appl. Phys. Lett.* **2014**, *104*, 251915.
- (26) Jiang, J.-W.; Park, H. S. Negative Poisson's Ratio in Single-Layer Black Phosphorus. *Nat. Commun.* **2014**, *5*, 4727.
- (27) Takao, Y.; Asahina, H.; Morita, A. Electronic Structure of Black Phosphorus in Tight Binding Approach. *J. Phys. Soc. Japan* **1981**, *50*, 3362–3369.
- (28) Tran, V.; Soklaski, R.; Liang, Y.; Yang, L. Layer-Controlled Band Gap and Anisotropic Excitons in Few-Layer Black Phosphorus. *Phys. Rev. B* **2014**, *89*, 235319.
- (29) Zhang, J.; Liu, H. J.; Cheng, L.; Wei, J.; Liang, J. H.; Fan, D. D.; Jiang, P. H.; Sun,

- L.; Shi, J. High Thermoelectric Performance Can Be Achieved in Black Phosphorus. *J. Mater. Chem. C* **2016**, *4*, 991–998.
- (30) Zhu, L.; Zhang, G.; Li, B. Coexistence of Size-Dependent and Size-Independent Thermal Conductivities in Phosphorene. *Phys. Rev. B* **2014**, *90*, 214302.
- (31) Jain, A.; McGaughey, A. J. H. Strongly Anisotropic in-Plane Thermal Transport in Single-Layer Black Phosphorene. *Sci. Rep.* **2015**, *5*, 8501.
- (32) Qin, G.; Yan, Q.-B.; Qin, Z.; Yue, S.-Y.; Hu, M.; Su, G. Anisotropic Intrinsic Lattice Thermal Conductivity of Phosphorene from First Principles. *Phys. Chem. Chem. Phys.* **2015**, *17*, 4854–4858.
- (33) Luo, Z.; Maassen, J.; Deng, Y.; Du, Y.; Garrelts, R. P.; Lundstrom, M. S.; Ye, P. D.; Xu, X. Anisotropic in-Plane Thermal Conductivity Observed in Few-Layer Black Phosphorus. *Nat. Commun.* **2015**, *6*, 8572.
- (34) Lee, S.; Yang, F.; Suh, J.; Yang, S.; Lee, Y.; Li, G.; Sung Choe, H.; Suslu, A.; Chen, Y.; Ko, C.; *et al.* Anisotropic in-Plane Thermal Conductivity of Black Phosphorus Nanoribbons at Temperatures Higher than 100 K. *Nat. Commun.* **2015**, *6*, 8573.
- (35) Jang, H.; Wood, J. D.; Ryder, C. R.; Hersam, M. C.; Cahill, D. G. Anisotropic Thermal Conductivity of Exfoliated Black Phosphorus. *Adv. Mater.* **2015**, *27*, 8017–8022.
- (36) Zhu, J.; Park, H.; Chen, J.-Y.; Gu, X.; Zhang, H.; Karthikeyan, S.; Wendel, N.;

- Campbell, S. A.; Dawber, M.; Du, X.; *et al.* Revealing the Origins of 3D Anisotropic Thermal Conductivities of Black Phosphorus. *Adv. Electron. Mater.* **2016**, *2*, 10.1002/aelm.201600040.
- (37) Sugai, S.; Shirotani, I. Raman and Infrared Reflection Spectroscopy in Black Phosphorus. *Solid State Commun.* **1985**, *53*, 753–755.
- (38) Wu, J.; Mao, N.; Xie, L.; Xu, H.; Zhang, J. Identifying the Crystalline Orientation of Black Phosphorus Using Angle-Resolved Polarized Raman Spectroscopy. *Angew. Chemie* **2015**, *127*, 2396–2399.
- (39) Wood, J. D.; Wells, S. A.; Jariwala, D.; Chen, K.-S.; Cho, E.; Sangwan, V. K.; Liu, X.; Lauhon, L. J.; Marks, T. J.; Hersam, M. C. Effective Passivation of Exfoliated Black Phosphorus Transistors against Ambient Degradation. *Nano Lett* **2014**, *14*, 6964.
- (40) Island, J. O.; Steele, G. A.; Zant, H. S. J. van der; Castellanos-Gomez, A. Environmental Instability of Few-Layer Black Phosphorus. *2D Mater.* **2015**, *2*, 011002.
- (41) Ziletti, A.; Carvalho, A.; Campbell, D. K.; Coker, D. F.; Castro Neto, A. H. Oxygen Defects in Phosphorene. *Phys. Rev. Lett.* **2015**, *114*, 26–29.
- (42) Lv, H. Y.; Lu, W. J.; Shao, D. F.; Sun, Y. P. Enhanced Thermoelectric Performance of Phosphorene by Strain-Induced Band Convergence. *Phys. Rev. B* **2014**, *90*,

085433.

- (43) Cai, W.; Moore, A. L.; Zhu, Y.; Li, X.; Chen, S.; Shi, L.; Ruoff, R. S. Thermal Transport in Suspended and Supported Monolayer Graphene Grown by Chemical Vapor Deposition. *Nano Lett.* **2010**, *10*, 1645–1651.
- (44) Hsu, I. K.; Kumar, R.; Bushmaker, A.; Cronin, S. B.; Pettes, M. T.; Shi, L.; Brintlinger, T.; Fuhrer, M. S.; Cumings, J. Optical Measurement of Thermal Transport in Suspended Carbon Nanotubes. *Appl. Phys. Lett.* **2008**, *92*, 7–9.
- (45) Zhou, H.; Zhu, J.; Liu, Z.; Yan, Z.; Fan, X.; Lin, J.; Wang, G.; Yan, Q.; Yu, T.; Ajayan, P. M.; *et al.* High Thermal Conductivity of Suspended Few-Layer Hexagonal Boron Nitride Sheets. *Nano Res.* **2014**, *7*, 1232–1240.
- (46) Yan, R.; Simpson, J. R.; Bertolazzi, S.; Brivio, J.; Watson, M.; Wu, X.; Kis, A.; Luo, T.; Hight Walker, A. R.; Xing, H. G. Thermal Conductivity of Monolayer Molybdenum Disulfide Obtained from Temperature-Dependent Raman Spectroscopy. *ACS Nano* **2014**, *8*, 986–993.
- (47) Kim, P.; Shi, L.; Majumdar, A.; McEuen, P. L. Thermal Transport Measurements of Individual Multiwalled Nanotubes. *Phys. Rev. Lett.* **2001**, *87*, 215502.
- (48) Shi, L.; Li, D. Y.; Yu, C. H.; Jang, W. Y.; Kim, D.; Yao, Z.; Kim, P.; Majumdar, A. Measuring Thermal and Thermoelectric Properties of One-Dimensional Nanostructures Using a Microfabricated Device. *J. Heat Transf. Asme* **2003**, *125*,

881–888.

- (49) Li, D.; Wu, Y.; Kim, P.; Shi, L.; Yang, P.; Majumdar, A. Thermal Conductivity of Individual Silicon Nanowires. *Appl. Phys. Lett.* **2003**, *83*, 2934–2936.
- (50) Pettes, M. T.; Jo, I.; Yao, Z.; Shi, L. Influence of Polymeric Residue on the Thermal Conductivity of Suspended Bilayer Graphene. *Nano Lett.* **2011**, *11*, 1195–1200.
- (51) Jo, I.; Pettes, M. T.; Ou, E.; Wu, W.; Shi, L. Basal-Plane Thermal Conductivity of Few-Layer Molybdenum Disulfide. *Appl. Phys. Lett.* **2014**, *104*, 201902.
- (52) Mavrokefalos, A.; Pettes, M. T.; Zhou, F.; Shi, L. Four-Probe Measurements of the in-Plane Thermoelectric Properties of Nanofilms. *Rev. Sci. Instrum.* **2007**, *78*, 034901.
- (53) Cahill, D. G.; Goodson, K. E.; Majumdar, A. Thermometry and Thermal Transport in Micro/Nanoscale Solid-State Devices and Structures. *J. Heat Transfer* **2001**, *124*, 1–19.
- (54) Cahill, D. G. Analysis of Heat Flow in Layered Structures for Time-Domain Thermoreflectance. *Rev. Sci. Instrum.* **2004**, *75*, 5119–5122.
- (55) Feser, J. P.; Liu, J.; Cahill, D. G. Pump-Probe Measurements of the Thermal Conductivity Tensor for Materials Lacking in-Plane Symmetry. *Rev. Sci. Instrum.* **2014**, *85*.

- (56) Liu, J.; Choi, G. M.; Cahill, D. G. Measurement of the Anisotropic Thermal Conductivity of Molybdenum Disulfide by the Time-Resolved Magneto-Optic Kerr Effect. *J. Appl. Phys.* **2014**, *116*, 233107.
- (57) Kim, J.; Ou, E.; Sellan, D. P.; Shi, L. A Four-Probe Thermal Transport Measurement Method for Nanostructures. *Rev. Sci. Instrum.* **2015**, *86*, 044901.
- (58) Kim, J.; Evans, D. A.; Sellan, D. P.; Williams, O. M.; Ou, E.; Cowley, A. H.; Shi, L. Thermal and Thermoelectric Transport Measurements of an Individual Boron Arsenide Microstructure Thermal and Thermoelectric Transport Measurements of an Individual Boron Arsenide Microstructure. *Appl. Phys. Lett.* **2016**, *108*, 201905.
- (59) Ou, E. Four-Probe Thermal Measurement of a Carbon Nanotube Sheet, The University of Texas at Austin, 2015.
- (60) Jo, I.; Pettes, M. T.; Lindsay, L.; Ou, E.; Weathers, A.; Moore, A. L.; Yao, Z.; Shi, L. Reexamination of Basal Plane Thermal Conductivity of Suspended Graphene Samples Measured by Electro-Thermal Micro-Bridge Methods. *AIP Adv.* **2015**, *5*, 053206.
- (61) Liu, X.; Wood, J. D.; Chen, K.-S.; Cho, E.; Hersam, M. C. In Situ Thermal Decomposition of Exfoliated Two-Dimensional Black Phosphorus. *J. Phys. Chem. Lett.* **2015**, *6*, 773–778.
- (62) Shi, L.; Li, D.; Yu, C.; Jang, W.; Kim, D.; Yao, Z.; Kim, P.; Majumdar, A.

- Measuring Thermal and Thermoelectric Properties of One-Dimensional Nanostructures Using a Microfabricated Device. *J. Heat Transfer* **2003**, *125*, 881.
- (63) Gang, C. Nanoscale Energy Transport and Conversion. In; Oxford University Press, 2005; pp. 245–246.
- (64) Kittel, C. Introduction to Solid State Physics. In; John Wiley & Sons, Inc, 2004; pp. 125–128.
- (65) Li, W.; Carrete, J.; Katcho, N. A.; Mingo, N. ShengBTE: A Solver of the Boltzmann Transport Equation for Phonons. *Comput. Phys. Commun.* **2014**, *185*, 1747–1758.
- (66) Kresse, G.; Furthmüller, J. Efficient Iterative Schemes for Ab Initio Total-Energy Calculations Using a Plane-Wave Basis Set. *Phys. Rev. B* **1996**, *54*, 11169–11186.
- (67) Blöchl, P. E. Projector Augmented-Wave Method. *Phys. Rev. B* **1994**, *50*, 17953–17979.
- (68) Farrell, R. A.; Petkov, N.; Shaw, M. T.; Djara, V.; Holmes, J. D.; Morris, M. A. Monitoring PMMA Elimination by Reactive Ion Etching from a Lamellar PS-B-PMMA Thin Film by Ex Situ TEM Methods. *Macromolecules* **2010**, *43*, 8651–8655.
- (69) Yabumoto, N.; Oshima, M.; Michikami, O.; Yoshi, S. Surface Damage on Si Substrates Caused by Reactive Sputtering Etching. *Jpn. J. Appl. Phys.* **1981**, *20*, 893.

- (70) Pang, S. W.; Rathman, D. D.; Silversmith, D. J.; Mountain, R. W.; DeGraff, P. D. Damage Induced in Si by Ion Milling or Reactive Ion Etching. *J. Appl. Phys.* **1983**, *54*, 3272–3277.
- (71) Heinbach, M.; Kaindl, J.; Franz, G. Lattice Damage in III/V Compound Semiconductors Caused by Dry Etching. *Appl. Phys. Lett.* **1995**, *67*, 2034.
- (72) Sahoo, S.; Gaur, A. P. S.; Ahmadi, M.; Guinel, M. J. F.; Katiyar, R. S. Temperature-Dependent Raman Studies and Thermal Conductivity of Few-Layer MoS<sub>2</sub>. *J. Phys. Chem. C* **2013**, *117*, 9042–9047.